Cosmological Tests of Causal Set Phenomenology

by

Nosiphiwo Zwane

A thesis
presented to the University of Waterloo
in fulfillment of the
thesis requirement for the degree of
Doctor of Philosophy
in
Physics

Waterloo, Ontario, Canada, 2017

Examining Committee Membership

The following served on the Examining Committee for this thesis. The decision of the Examining Committee is by majority vote.

External Examiner:	Professor Jennie Traschen
Supervisor:	Professor Rafael Sorkin
Co-Supervisor:	Professor Niayesh Afshordi
Internal Member:	Professor Robert Mann
Internal Member:	Professor Robert Myers
Internal/External Examiner:	Professor Achim Kempf

This thesis consists of material all of which I authored or co-authored: see Statement of Contributions included in the thesis. This is a true copy of the thesis, including any required final revisions, as accepted by my examiners.

I understand that my thesis may be made electronically available to the public.

Statement of Contributions

The research presented in this thesis consists of these papers:

- Zwane, Nosiphiwo, Niayesh Afshordi, Rafael D Sorkin, 2017. Cosmological test of Everpresent Λ,*arXiv:1703.06265*
- Rafael D Sorkin, Zwane, Nosiphiwo, *in preparation*, Distance Between of Lorentzian Spacetimes and the Hauptvermutung of Causal Set Theory.
- Rafael D Sorkin , Zwane, Nosiphiwo, *in preparation*, Anti-de Sitter spacetime as the limit of causal sets.

Abstract

Causal Set Theory is an approach to Quantum Gravity that postulates that the fundamental structure of a spacetime manifold is a Lorentz invariant discrete structure endowed with a causal order from which the geometry and topology of the spacetime can be recovered. The continuum emerges as an approximation at macroscopic scales.

Lorentz invariant discreteness can have consequences that can be observed at low energies. In this work, we search for signatures of causal set predictions. Causal Set Theory predicts that the cosmological constant Λ is Everpresent and fluctuates between positive and negative values. This cosmological model, a stochastic function of cosmic time that varies from one realization to another, generates a space of histories of dark energy. Via Monte Carlo Markov chains we search the space of histories of dark energy to find the best fit to Cosmic Microwave Background (CMB) data, Big Bang Nucleosynthesis (BBN) data and Baryon acoustic oscillations (BAO) data. The model fits the current cosmological observations well and eases the tension that standard ΛCDM has at high redshift.

Causal Set Theory also predicts that a particle propagating on a causal set will undergo diffusion in momentum space. For massive particles, the diffusion process has only one parameter, the diffusion constant. For massless particles this process has two parameters − the diffusion constant and the drift parameter. These parameters depend on the non-locality scale of the theory. Simulations were run to find the relation between these parameters and the non-locality scale. There by using bounds on the diffusion constant, we set bounds on the non-locality scale.

Acknowledgements

I would like to thank the Perimeter Institute for Theoretical Physics and the University of Waterloo for hosting me during my PhD. First and foremost, I would like to thank my supervisor, Rafael Sorkin, for giving me advice and guidance throughout my PhD. I appreciate your ability to explain complicated ideas in simple ways. Thank you to my co-supervisor Niayesh Afshordi for always making time to meet with me answer my questions. Thank you to the members of my advisory committee: Achim Kempf, Robert Mann, Robert Meyers, for offering valuable insight and comments on my research throughout my PhD.

Thank you to all the member of our research group: Siavash Aslanbeigi, Mehdi Saravani, Yasaman Yazdi, Daniel Guariento, Natacha Altamirano, Mansour Karami, Chiamaka Okoli and Beth Gould and Farbod Kamiab, for the informative discussions that helped broaden my knowledge in different areas of physics. Thank you to the causal set community, for the informative discussion I have had over the years with Fay Dowker, Sumati Surya, David Rideout, Lisa Glaser.

Thank you to all my friends who have been my Canadian family away from home for the past years. Last but not least, I would like to thank my family for their support throughout my PhD.

Dedication

This is dedicated to my father.

Table of Contents

List of Tables

List of Figures

Chapter 1

Introduction

The search for theories for the five forces of nature (Higgs, weak, strong, electromagnetic, and gravity) goes back centuries. The Standard Model is the most successful quantum theory of the first four forces and has existed for years. Its problems are the infinities, which seem to require a cut-off at small scales, suggesting an existence of minimum length. In Quantum Field Theory renormalization is used to partly handle this problem, which returns in direct attempts to quantising gravity. Renormalization still leaves the technical problems that arise in defining the path-integral on a continuous history space not fully resolved. A discrete history space provides a well−defined path integral, or a sum over histories, that avoids these problems.

The well−known theory of gravity, General Relativity, has singularities suggesting a fundamental minimum length. Sorkin[2] showed that for the blackhole entropy to agree with semi-classical results a minimum length scale must be introduced. Also resolving distance between arbitrarily close spacetime events is impossible since by the uncertainty principle this would require too much energy. These problems suggest that at high energies the continuum spacetime approach fails, leading one to believe the fundamental underlying theory is atomically discrete. This atomic discreteness provides the necessary cut-off to degrees of freedom at small scales. It is worth considering that atomic discreteness could never be found, for instance, by quantising some effective continuum theory, but must instead have an independent hypothesis.

The question of interest then becomes the choices of postulates to use in building a fundamental theory that is most likely to give the correct theory, according to known physics. For example, in assuming that fundamental structure is discrete, one has to worry about the theory being Lorentz invariant, as astrophysical observations[3] have placed tight

bounds on Lorentz Invariance violation.

The standard definition of Lorentz Invariance only has meaning in the continuum approximation. A discrete structure maybe considered to be Locally Lorentz invariant if the underlying structure does not pick a preferred direction. For example a regular lattice structure will violate Local Lorentz Invariance while something like an ideal gas because it is randomly distributed, has no preferred direction and will not violate Local Lorentz Invariance. For the underlying discrete theory to be Lorentz invariant, it cannot be a regular lattice but rather a random distribution.

Spacetime causal order is an important feature of General Relativity. In a Lorentzian spacetime Manifold $\mathcal{M}$ with metric g, the causal future of a point $x \in \mathcal{M}$ is the set of all points that are on a future directed causal curve from x, denoted by $J^+(x)$. Similarly, the past of $x \in \mathcal{M}$ is the set of all points that are on a past directed causal curve from x, denoted by $J^-(x)$. The causal structure of the spacetime $(\mathcal{M}, g)$ is the collection of $J^+(x)$ and $J^-(x)$ for all $x \in \mathcal{M}$.

Theorems by Robb[4], Zeeman[5], Hawking *et al.*[6], Malament[7] and Levichev[8] point out that for continuum spacetime, from the causal structure one can recover the topology of the spacetime and the geometry of the spacetime up to a conformal factor. This idea suggests that the fundamental structure of spacetime is the causal structure. Causal set theory uses the two ideas that spacetime is fundamentally discrete and that the fundamental structure is the causal structure.

Many researchers have independently been led to the same hypothesis [9, 10, 11]: that the causal set should be the structure that replaces the continuum manifold. A causal set is a locally finite set of elements endowed with a partial order corresponding to causal relations. The order relations give the causal structure and the number of elements corresponds to the volume. Sorkin's slogan summarizes this idea and states that

$$\text{Spacetime Geometry} \approx \text{Order} + \text{Number}.$$

Lorentz invariant discreteness can have consequences that can be observed at low energies. Searching for signatures for such consequences even without a fully developed theory of quantum gravity can lead to many interesting directions, and also serve as evidence for the postulates of the theory. For example, if Lorentz breaking were to be detected today it would not favor this theory.

The number volume correspondence in causal sets is not exact but subject to fluctuations since the causal elements are to be randomly distributed for the theory to be Lorentz invariant. The term that involves the cosmological constant in the Einstein-Hilbert action

is $-\int \Lambda dV$, suggesting that V and Λ are canonical conjugates. Sorkin *et al.*[12] argued that the cosmological constant will be present at all times and will fluctuate, with the fluctuations being proportional to the inverse of the square root of volume, $\Delta\Lambda \sim V^{-1/2}$. Assuming $\langle\Lambda\rangle = 0$ (i.e. a yet-unknown solution to the old cosmological constant problem), and taking volume to be roughly the fourth power of the Hubble radius, H^{-1}, Sorkin[13] predicted that the cosmological constant is

$$\Lambda \sim H^2 = \frac{1}{3}\rho_c, \tag{1.1}$$

where ρ_c is the critical energy density of the universe. This prediction yields the correct order of magnitude of the cosmological constant.

This model of dark energy is different from the standard ΛCDM (Lambda cold dark matter) model, as it has everpresent Λ that fluctuates between positive and negative values with a vanishing mean, and with a magnitude comparable to the critical density at any epoch. Λ is a stochastic function of cosmic time that will vary from one realization to another. In Chapter 2, we consider two models of "dark energy" that exhibit these features. Via Monte Carlo Markov chains, we explore the space of cosmological parameters and the set of stochastic realizations of these models, finding that Everpresent Λ can fit the current cosmological observations as well as the ΛCDM model does. Furthermore, Everpresent Λ can potentially ease some high redshift tensions with ΛCDM, including the Baryonic Acoustic Oscillations (BAO) in Lyman-α forest at $z \sim 2-3$, the ultra-massive black holes at $z \sim 7$, and the primordial Lithium-7 abundance that is set at $z \sim 1010$.

The causal set hypothesis makes a definite statement that the fundamental structure of a spacetime manifold is discrete and Lorentz invariant, that is the causal elements are randomly distributed. A particle propagating on a causal set will not travel on an exact geodesic but will have to swerve jumping from one causal element to the next like a random walk. This phenomenology has been studied by several people in References[14, 15, 16]. The worldline fluctuations can be modelled as diffusion with only one parameter, the diffusion constant. The diffusion is in momentum space. The particle will try to propagate on an exact geodesics to decrease change in momentum. Unlike a random walk, this process is approximately Markovian as the particle is given a small memory or forgetting time, τ_f. The larger τ_f is, the closer the trajectory will be to a geodesic. The forgetting time is related to the non-locality scale. In Chapter 3, we do simulations to find relationship between the diffusion constant and the non-locality scale and then use bounds on the diffusion constant to set bounds on the non-locality scale.

At microscopic scales, one would like to have the emergent spacetime manifold to be isometric to the General Relativity spacetime for our universe. To know how similar the

two spacetimes are requires a measure between the two spacetimes– general relativity spacetime and the spacetime emerging as an approximation from the fundamental structure. However, one might argue that such a measure is not important but getting the low energy observable from the fundamental theory should be enough. While this is true, for some of the low energy observable one would expect a deviation from the classical results when calculations are done in the fundamental theory. For such circumstances such a measure would be useful. In Chapter 4, we discuss a measure between two spacetime manifolds based on the "main conjecture" of causal sets. The main conjecture states that if two spacetime manifolds are an approximation of the same causal set, then these two manifolds should be isometric upto the discretization scale of the causal set.

1.1 Causal Set Review

A causal set[11] C is a discrete partially ordered set with elements related by a causal relation $\prec$, where $x \prec y$ implies that x is the parent (or an ancestor or is in the past) of y. The elements of a causal set satisfy the following axioms:

(i) Irreflexivity: $x \not\prec x, \forall x \in C$;

(ii) Transitivity: If $x \prec y$ and $y \prec z$ then $x \prec z$, $\forall x, y, z \in C$;

(iii) Local finiteness: $\forall x, z \in C$ the set $\{y | x \prec y \prec z\}$ is finite.

The first two axioms encode the causal order relations, which correspond to the causal structure. The third axiom, local finiteness is mathematically equivalent to discreteness. Irreflexivity ensures that causal cycles are not allowed, that is, for $x_i \in C$, $x_1 \prec x_2 \prec x_3 \ldots \prec x_1$ is not allowed since transitivity would then imply $x_1 \prec x_1$, which violates the first axiom.

A causal set has many representations. It can be represented as a graph called the Hasse diagram as shown in Figure 1.1. The causal elements are represented by vertices. If two elements are causally related, an edge joining the two vertices is added. In the Hasse diagram only relations that are not implied by transitivity are drawn. These relations are called *links*, denoted by $x \prec_* y$. A totally ordered subset of a causal set is called a *chain*, and an example is the chain $a \prec b \prec c \prec d$ in Figure 1.1.

A collection of unrelated elements in a causal set is called an *anti-chain*, such as $\{a, e, f\}$ in Figure 1.1. A *longest chain* between two elements is a chain whose length is maximal

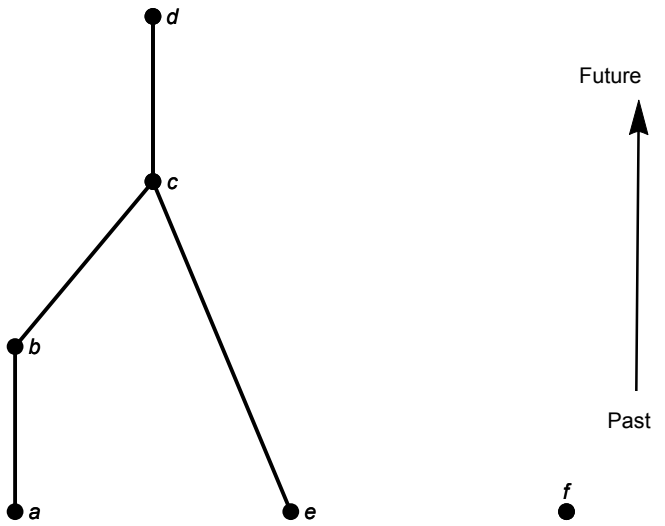

Figure 1.1: Hasse diagram for a six element causal set. Only relations that are not implied by transitivity are drawn.

among chains connecting the two elements. The length of the longest chain between x and y is denoted by $d(x, y)$. A *Time-like geodesic* is the longest chain. In Minkowski spacetime, $d(x, y) \sim \alpha T$, where T is the proper time and α is a dimension dependent constant. A *path* is a chain consisting entirely of links. An element $x \in C$ is called a *minimal* element if it has no element in its past, that is, $\nexists y \in C$ such that $y \prec x$. Examples of minimal elements are a, e and f in Figure 1.1. $x \in C$ is called *maximal* if $\nexists y \in C$ such that $x \prec y$, and an example is the element d in Figure 1.1.

A causal set can also be represented by a matrix. Consider a causal set that has its elements labelled in some order, x_i, where i is the index. Then the causal set can be represented as a link matrix, A_c or a causal matrix, A_R, such that

$$(A_R)_{ij} = \begin{cases} 1 & \text{if } x_i \prec x_j \\ 0 & \text{else} \end{cases} \qquad (A_C)_{ij} = \begin{cases} 1 & \text{if } x_i \prec_* x_j \\ 0 & \text{else} \end{cases} . \tag{1.2}$$

Having discussed the advantages of a causal set theory, the procedure to construct a causal set as a partial ordered set of histories with dynamics that would be a satisfying theory of quantum gravity remains an open problem. For a classical causal set, Sorkin and Rideout[17] proposed a sequential growth model. Not all causal sets have a continuum approximation at microscopic scales. A causal set that has a continuum approximation at macroscopic scales can be generated using *sprinkling*.

Sprinkling is a stochastic process of generating a causal set from a given spacetime manifold by randomly distributing points on the given manifold using the Poisson distribution with constant finite density ρ. The points become the causal elements without co-ordinates endowed with causal relations induced by the sprinkled manifold. This process gives a causal set that one can be sure in the continuum is approximated by a spacetime manifold. All causal sets used in this work will be generated using a sprinkling, though this seems circular in that we start from the continuum spacetime and generate a causal set, only to turn back and say the continuum spacetime is only an approximation of a causal set. We hope that in the full theory, the dynamics will generate a causal set without using the continuum spacetime, akin to the sequential growth model.

Chapter 2

Everpresent Lambda

In causal set theory, the number of causal elements corresponds to volume in the continuum. This correspondence is not exact if Lorentz Invariance holds but is subject to Poisson fluctuation. Relating the cosmological constant to the volume, led to the prediction that the cosmological constant will not be a constant, but will be subject to Poisson fluctuation. This model of dark energy is called Everpresent Lambda. Everpresent Lambda predicts that the "cosmological constant" fluctuates between positive and negative values with a vanishing mean. This implies that the "cosmological constant" is a stochastic function of cosmic time, with a standard deviation comparable to the critical density of the universe [18, 19, 20, 21, 22, 12, 23, 13, 24]. Work in this chapter is based on this paper [95].

The fluctuations are quantum mechanical results of spacetime being fundamentally discrete, which entails uncertainties in volume. Since the cosmological "constant" Λ is a function of time (and in principle, space) the Einstein's field equation for General Relativity 2.5 do not hold.

In this chapter, we discuss some cosmological tests of one possible model of these fluctuations, and show that the model agrees with current cosmology data and can ease some high redshift tensions with standard ΛCDM model.

In Section 2.1, we discuss stochastic phenomenological models of everpresent Λ, or dark energy, which satisfies the broad expectations from causal sets and quantum gravity. Moreover, model 2 admit a fully covariant and causal perturbation theory, allowing us to make predictions for cosmic microwave background (CMB) anisotropies.

In Section 2.2, we fit the model to the cosmic microwave background, using Planck 2015 data. Even though everpresent Λ is a stochastic model, a Monte Carlo exploration

of the space of likely dark-energy histories using the CAMB code finds several histories that are excellent fits to the Planck 2015 data. This does not fix the model to one good history of dark energy, but it does select a set of histories which fit the data, if $\Omega_{de} \simeq 0.7$ (0) at $z \simeq 0$ (1000), at 5% level. Since everpresent Λ is a stochastic model, we pay special attention to how one should compare it to conventional deterministic dark-energy models, and to what extent good fits are (or will be) contrived.

Section 2.3 compares everpresent Λ predictions for volume weighted distance D_v with Baryon acoustic oscillations (BAO) data from several surveys. BAO measurements provide an independent measure of expansion of the universe which complements supernovae data [25] in tests of dark energy models. In particular, the Baryon Oscillation Spectroscopic Survey (BOSS) results [26, 27] suggest that $\Omega_{de}(z)$ is negative at $z = 2.34$ at about 2.5σ tension with standard ΛCDM. A number of other models that Aubourg*et al.* [1] examined fail to fit the 2013 BAO data, unless one assumes that $\Omega_{de} < 0$ at $z \sim 2 - 3$. This is encouraging for everpresent Λ, since it allows for $\Omega_{de}(z)$ to switch sign roughly once a Hubble time.

In Section 2.4, we ask whether everpresent Λ can resolve the difficulty that ΛCDM is thought to have with the occurrence of ultra-massive black holes at high redshift. Quasar black holes at $z \sim 6$ to 7 have more mass than they are expected to, if one assumes ΛCDM cosmology and standard and/or plausible astrophysics (sub-Eddington accretion rates[28], maximal angular velocity of the black holes). Exotic astrophysical processes may increase the accretion rate, allowing the quasars to accumulate mass faster, but such processes have not been observed. Instead, we find that alternative dark energy histories, as are typical for everpresent Λ, can stretch the accretion time at high redshifts, and thus provide a simple (though incomplete) solution to this potential problem.

In Section 2.5, we discuss everpresent Λ as a cosmological solution to the primordial Lithium-7 problem. Big Bang Nucleosynthesis (BBN), predicts the abundance of light cosmological elements (D,^{3}He,^{4}He,^{7}Li) that are produced within the first 20 minutes after the Big Bang. The abundances of primordial Deuterium and Helium-4 predicted by BBN are in agreement with astronomically observed abundances. However BBN in a standard ΛCDM cosmology predicts about three times more Lithium-7 than is observed. We show that everpresent Λ can ease this tension, even though it cannot completely remove it if we take current astrophysical measurement errors at face value. Let us first briefly review the everpresent Λ hypothesis.

2.1 Everpresent Λ

The prediction that the cosmological "constant" should vary stochastically was an early heuristic prediction of causal set theory [18, 19, 20, 21, 22]. A concrete model of such an Everpresent Λ was first proposed by Ahmed *et al.* [12]. In causal set theory the number of elements determines the spacetime volume. The equality between number and volume is not exact if Lorentz Invariance holds, but is subject to Poisson fluctuations. In Planck units ($8\pi G = \hbar = c = 1$)

$$N \sim V \pm \sqrt{V}. \tag{2.1}$$

The term that involves the cosmological constant in the Einstein-Hilbert action is $-\int \Lambda dV$, suggesting that V and Λ are canonical conjugates [12]. Therefore, based on Heisenberg uncertainty principle, the quantum fluctuations would obey

$$\Delta\Lambda \times \Delta V \sim 1. \tag{2.2}$$

Holding the number of causal elements, N, fixed does not imply that the volume, V is fixed, hence it follows from equations (2.1) and (2.2) that

$$\Delta\Lambda \sim V^{-1/2}. \tag{2.3}$$

Assuming $< \Lambda >= 0$ and taking volume to be roughly the fourth power of the Hubble radius, H^{-1}

$$\Lambda \sim H^2 = \frac{1}{3}\rho_c. \tag{2.4}$$

Where ρ_c is the critical energy density of the universe. In conclusion, causal set theory predicts that the cosmological "constant" is of order H^2 and is everpresent and also fluctuates due to Poisson statistics of spacetime causal elements. For General Relativity field equations 2.5 to hold

$$G^{ab} + \Lambda g^{ab} = T^{ab}, \qquad \nabla_a T^{ab} = 0 \tag{2.5}$$

Λ must be a constant. To interpret the time dependence of Λ requires non-classically field equations or supplement cosmological constant by a scalar field. Assuming that spacetime is homogeneous, isotropic and spatially flat,

$$ds^2 = -dt^2 + a(t)^2\left(dx^2 + dy^2 + dz^2\right), \tag{2.6}$$

leads to Friedmann equations,

$$\left(\frac{\dot{a}}{a}\right)^2 = \frac{1}{3}\rho + \frac{\Lambda}{3} \tag{2.7}$$

$$\frac{\ddot{a}}{a} = -\frac{1}{6}(\rho + 3p) + \frac{\Lambda}{3}. \tag{2.8}$$

If Λ is a function of t, then equation(2.7) and equation (2.8) and are incompatible. Only one of these equations or a linear combination can be used for dynamics of everpresent Λ. Ahmed and Sorkin [23] showed that equation(2.8) is unstable under small fluctuations from the true solution, therefore it cannot be used as dynamical guide for everpresent Λ models. Also a linear combination of equation(2.7) and equation (2.8) with "too much" of equation (2.8) will also be unstable and cannot be used as a dynamic guide. We will consider two models of everpresent Λ.

2.1.1 Model 1

Proposed by Ahmed *et al.* [12], this model assumes that the cosmological constant fluctuates due to Poisson fluctuations as discussed above. The universe is assumed to have volume, $V(t)$, at sometime t, one uses Friedmann equation(2.7) to evolve the scale factor to some time $a(t + \Delta t)$ and then calculate the 4-volume of the past lightcone using:

$$V(t) = \frac{4\pi}{3}\int_0^t dt'\, a(t')^3 \left(\int_0^{t'} dt'' \frac{1}{a(t'')}\right)^3, \tag{2.9}$$

$$N(t) = V(t)/\ell_p^2, \tag{2.10}$$

$$\Delta S(t) = \beta\xi\sqrt{N(t+1) - N(t)} \tag{2.11}$$

$$\rho_\Lambda(t+1) = \frac{S(t) + \Delta S(t)}{V(t)}. \tag{2.12}$$

The parameter β is related to the magnitude of the fluctuations. When β is too large the fluctuations in Ω_Λ are large resulting in a large negative dark energy density which in turn gives negative total energy density and the universe collapses before it gets to today. Therefore, β can not be too big. On the other hand, a small value of β will not give the correct value of Λ today.Ahmed *et al.* [12] found that $0.01 < \beta < 0.02$ to get a universe consistent with astrophysical observations. N_i is the number of causal elements at i^{th} iteration, ξ is a random number which drives the random walk and S is the action of free spacetime per unit volume (not including curvature term). Figure 2.1 shows Ω_{de} for this model.

2.1.2 Model 2

In this model, the cosmological constant is assumed to also fluctuate due to Poisson fluctuations resulting in correlation in cosmological constant at different times. We phenomenologically quantify these fluctuations by:

$$\left\langle \hat{\Omega}_{de}(\lambda_1)\hat{\Omega}_{de}(\lambda_2) \right\rangle = \alpha^2 e^{-\frac{\mu(\lambda_1-\lambda_2)^2}{2}} \tag{2.13}$$

where $\lambda = \log(a)$, a being the scale factor, α is the magnitude of the fluctuations and μ governs the autocorrelation-time of the fluctuations. Assuming a flat homogeneous cosmology and positive matter density, we require $\Omega_{de}(\lambda) < 1$ for all λ. Furthermore, assuming a symmetric distribution would imply $|\Omega_{de}(z)| < 1$. In order to ensure this, we adopt:

$$\Omega_{de}(\lambda) = \tanh\left[\hat{\Omega}_{de}(\lambda)\right]. \tag{2.14}$$

In other words, Ω_{de} is the hyperbolic tangent of a random Gaussian function of time, with zero mean and variance of α.

To simulate this model, we Fourier Transform the correlation to

$$\left\langle \tilde{\Omega}_{de}(\omega_1)\tilde{\Omega}_{de}(\omega_2) \right\rangle = \alpha^2 e^{-\frac{\omega^2}{4\mu}} \sqrt{\frac{\pi}{\mu}}\delta(\omega_1 - \omega_2). \tag{2.15}$$

We then sample $\tilde{\Omega}(\omega)_{de}$'s as independent Gaussian variables, and Fourier transform back to $\hat{\Omega}(\lambda)_{de}$, getting a random history of $\Omega_{de}(\lambda) = \tanh\hat{\Omega}(\lambda)_{de}$ as shown in Figure 2.1. Since $\hat{\Omega}_{de}$ is a random Gaussian function, the reduced $\chi^2_{red,\text{model}}$ for this model is given by

$$\chi^2_{red,\text{model}} = \frac{\chi^2_{\text{model}}}{\sum_\omega \#\omega} \sim 1 \pm \sqrt{\frac{2}{\#\omega}} \tag{2.16}$$

where $\#$ is the number of sampled ω's and,

$$\chi^2_{\text{model}} = \sum_\omega \frac{\left|\tilde{\Omega}_{de}(\omega)\right|^2}{\left\langle \left|\tilde{\Omega}_{de}(\omega)\right|^2 \right\rangle}. \tag{2.17}$$

In particular, we shall use the reduced chi-squared, $\chi^2_{red,\text{model}}$, as a measure of how typical the histories that fit observations may be in the context of everpresent Λ. This can then, in principle, be used to falsify our stochastic model.

This model is not intrinsic to causal set theory, it does not have any underlying dynamics but captures the general signature of everpresent Λ. It is easier to simulate than Model 1, and so we shall adopt it in our Monte Carlo Markov Chain (MCMC) exploration of the parameter space below. All cosmological tests use this model.

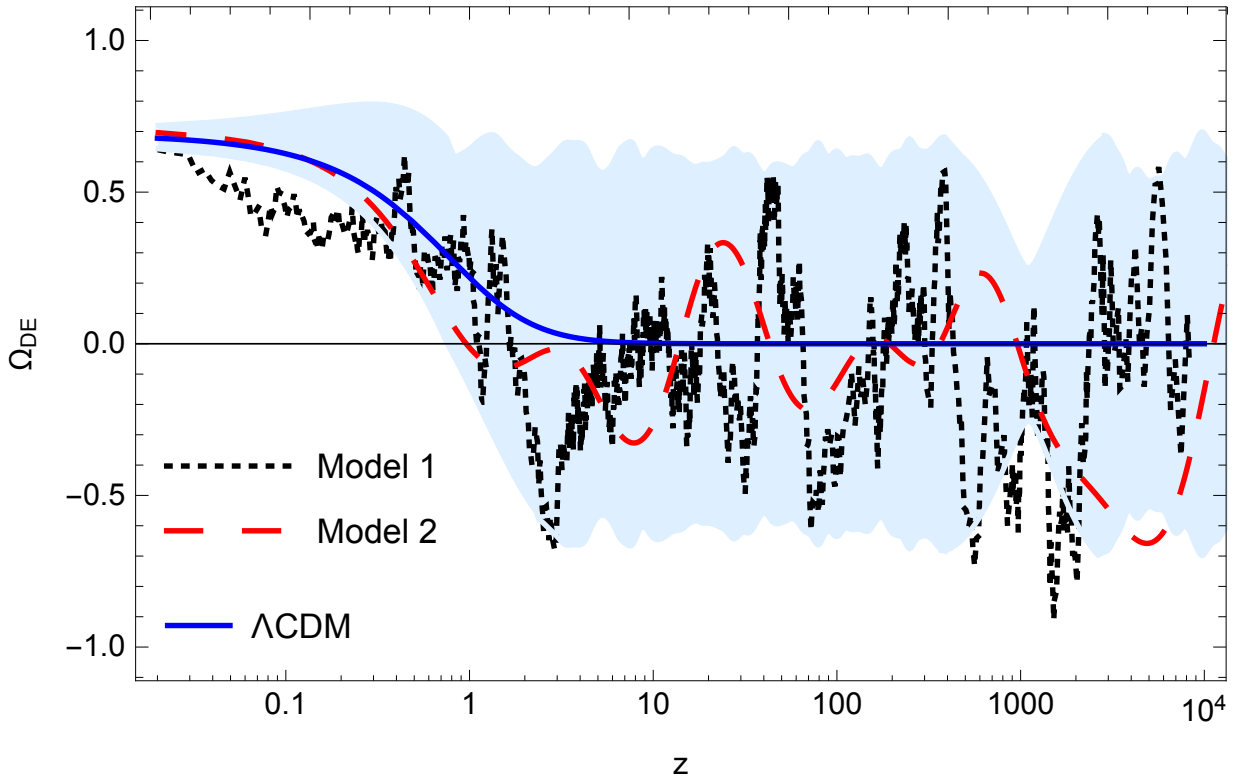

Figure 2.1: Dark Energy history, $\Omega_{de}(z)$, for two everpresent Λ models that fit Planck+BAO data, compared with ΛCDM model. The shaded area shows the 68% region of realizations of Model 2 that fit the data well.

2.1.3 Inhomogeneities

We live in an inhomogeneous universe. Therefore, any covariant model of a time-dependent dark energy also requires a consistent treatment of inhomogeneities. Based on this, Barrow [29] and Zuntz [30] argued for strong constraints on everpresent $\Lambda(t, \mathbf{x})$, with fluctuations less than 10^{-6}, which would make it irrelevant for cosmic acceleration today. Their argument used the assumption that, if Λ is determined by the Poisson fluctuations in the volume of the past light cones, then the correlation between $\Lambda(t, \mathbf{x})$ at points a and b will be related to the size of the intersection of the past light cones of a and b. Therefore, separate patches in the CMB sky will have uncorrelated Ω_Λ fluctuations, which limits the amplitude $\lesssim 10^{-6}$ from CMB observations. However, their treatment assumes a local stochastic notion for quantum fluctuations, which is not necessarily consistent with the non-local nature of quantum mechanics manifested, for example, by Bell inequalities [31].

We adopt a different approach. Assuming that dark energy is a perfect fluid with perturbations that propagate with the speed of light, consistent with the Lorentz symmetry of the underlying causal set. In the cosmological context, this is equivalent to a *quintessence* dark energy [32], which can be modelled by a scalar field with a canonical kinetic term. Then, fixing the history of the homogenous dark energy (using either Models 1 or 2 above), along with energy-momentum conservation and adiabatic initial conditions, uniquely fixes the behavior of linear perturbations.

This is not intrinsic to Causal Set Theory. However, it is a phenomenologically consistent and viable model that captures two main features expected in causal sets, i.e. everpresent Λ that fluctuate with time, and local Lorentz symmetry for inhomogeneities.

2.2 CMB and Everpresent Λ

Due to a combination of the quality of data and the validity of linear perturbation theory, the Cosmic Microwave Background (CMB) anisotropies currently provide the most precise tests of cosmological models. To fit everpresent Λ model, we use `CosmoMc` [33] and `CAMB` [34]. As this model of dark energy is stochastic, even the same values of α and μ could lead to vastly different geometries of the universe, resulting in e.g., different ages or present-day densities of dark energy. One way to quantify this is through the initial seed number, used to generate the pseudo-random numbers that go into $\Omega_{de}(z)$. Therefore, we shall run CosmoMC with $(\alpha, \mu, seed)$ as additional parameters included in the Monte-Carlo Markov Chain (MCMC). Note that, unlike other cosmological parameters, the likelihood surface will not be a smooth function of the *seed*. However, an MCMC random walk in this space

Cosmological Parameters	ΛCDM	Everprent Λ
$\Omega_b h^2$	0.02225 ± 0.00019	0.02205 ± 0.00021
$\Omega_c h^2$	0.11857 ± 0.0012	0.1208 ± 0.0026
$100\theta_{MC}$	1.04 ± 0.00040	1.041 ± 0.00063
τ	0.06782 ± 0.012	0.06903 ±0.014
n_s	0.9675 ± 0.0043	0.9593 ± 0.0064
$10^9 A_s$	2.146 ± 0.049	2.168 ± 0.066
Ω_Λ	0.6920 ± 0.0072	0.6781 ± 0.0081
H_0	67.79± 0.54	68.48 ± 0.67
Age/Gyr	13.80 ± 0.027	13.77 ± 0.031
α	–	0.8824
μ	–	0.9804
$\chi^2_{\text{model}-\text{data}}$	11334.6	11335.2

Table 2.1: Parameters for ΛCDM cosmology and cosmology with Everpresent Λ (model 2) computed from the 2015 baseline Planck (in combination with lensing reconstruction and BAO (6DF, MGS, DR11CMASS, DR11LOWZ, DR11LyaAuto, DR11LyaCross)) likelihoods, using CosmoMC. This illustrates the consistency of parameters determined from the temperature and polarization spectra at high multipoles.

will randomly sample various dark energy histories and keep the ones that fit the data well. While there is no guarantee that this chain converges quickly (or at all) due to the stochastic dependence of likelihood on the *seed* parameter, we see below that it does find fits to data comparable to standard ΛCDM cosmology.

Table 2.1 shows best fit parameters for both ΛCDM cosmology and cosmology with everpresent Λ. This shows that for α =0.8824 and μ = 0.9804 there exists a history of dark energy that is a good fit to the CMB + BAO. Figure 2.2 shows plot of anisotropy power spectrum, D_ℓ^{TT} vs ℓ for the different models.

To check how often one can get such a good fit from everpresent Λ, we look at the probability distribution of χ^2_{red} for everpresent Λ.

$$P\left[\chi^2_{red}(\tilde{\Omega}_{de})\right] \propto \int D\tilde{\Omega}'_{de} \exp\left(-\frac{\chi^2(\tilde{\Omega}'_{de})}{2}\right) \delta_D\left[\chi^2_{red}(\tilde{\Omega}'_{de}) - \chi^2_{red}(\tilde{\Omega}_{de})\right],$$

where $\chi^2_{red}(\tilde{\Omega}_{de})$ is given by Equation 2.17 (not to be confused with $\chi^2_{\text{model}-\text{data}}$ for fitting

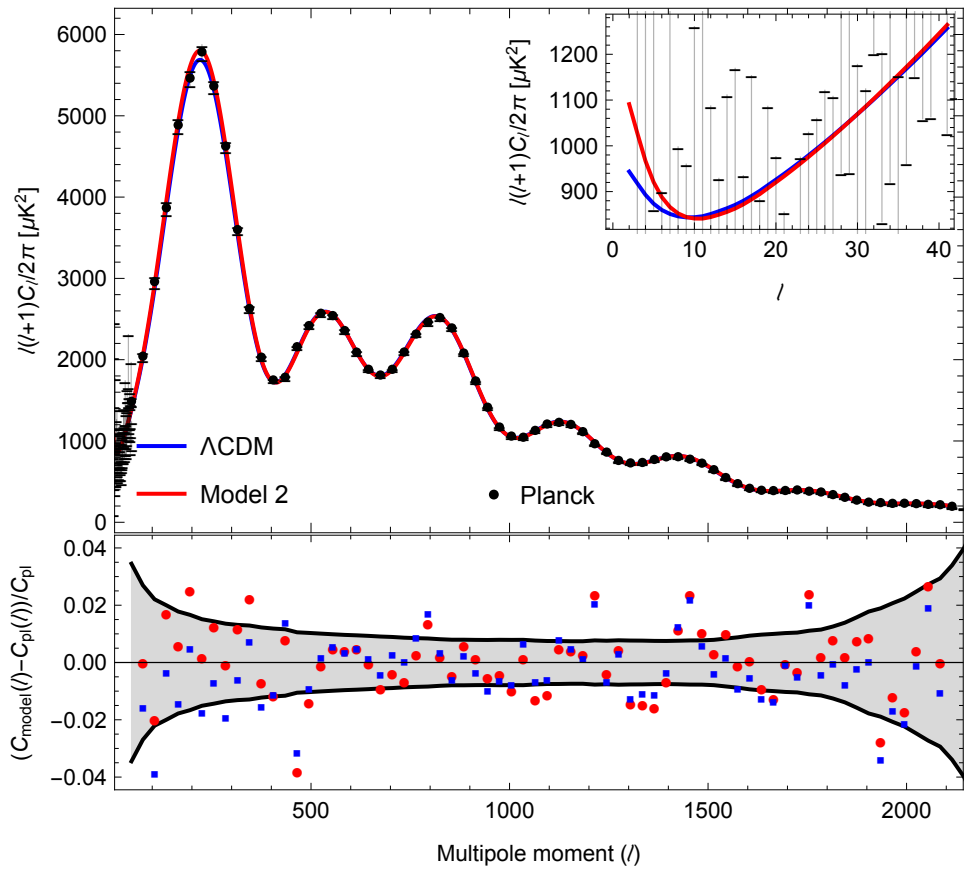

Figure 2.2: Temperature fluctuations for ΛCDM model and everpresent Λ models with parameters given in Table 2.1 and Planck 2015 data. The bottom plots show difference in temperature fluctuations from everpresent Λ, ΛCDM and Planck data.

	ΛCDM	Everpresent Λ
CMB: BKPLANCK	45.117	44.636
CMB: lensing	12.157	13.930
plik	1164.783	1165.278
lowTEB	10098.575	10097.773
BAO: 6DF	0.087	0.291
BAO: MGS	0.927	2.217
BAO: DR11CMASS	2.856	3.015
BAO: DR11LOWZ	1.098	1.442
BAO: DR11LyaAuto	4.265	2.636
BAO: DR11LyaCross	4.748	3.945
Total	11334	11335

Table 2.2: Breakdown of $\chi^2_{\text{model}-\text{data}}$'s into different datasets, for ΛCDM and best-fit everpresent Λ.

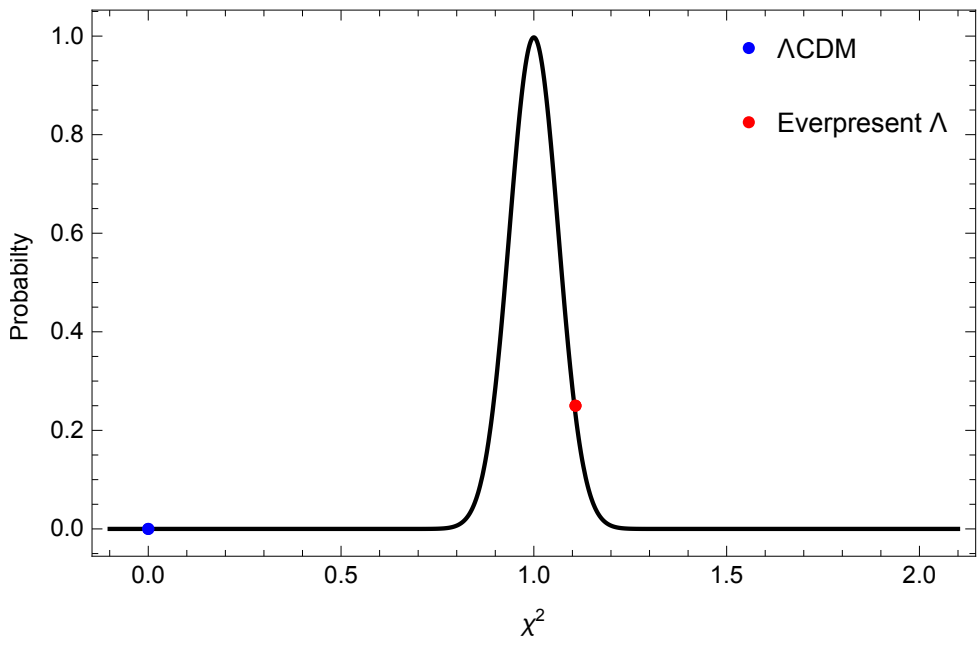

Figure 2.3: This shows that the best-fit history is a typical model-2 realization, whereas ΛCDM would be a very atypical outcome of model 2.

data in Tables 2.1-2.2). Figure 2.3 shows the expected χ^2_{red} distribution from gaussian statistics, as well as $\chi^2_{red}(\tilde{\Omega}_{de})$ for ΛCDM and best-fit everpresent Λ dark energy history $\tilde{\Omega}_{de}(z)$. ΛCDM has a small χ^2_{red} because most of $\tilde{\Omega}_{de}$ are zero. We see that the best fit everpresent Λ model is only 1.8σ away from the mean, while the ΛCDM sits well in the tail at $\sim 4.3\sigma$. This implies that the random Gaussian dark energy histories that fit the current data are not atypical based on χ^2 statistics. However, we will have to revise this assessment if future observations prefer histories closer and closer to ΛCDM.

Fixing the values of α =0.8824 and μ =0.9804, how likely is it to get a universe like ours in Figure 2.1, amongst all possible realizations? Since the typical value of $|\Omega_{de}|$ is 0.7 for this model, there is nothing unusual about the current density of dark energy. The only peculiar feature is that dark energy happens to be small ($|\Omega_{de}| < 0.1$) near last scattering, $z \simeq 1000$, where most the CMB signal is originated. However, given the value of α, this can happen with $\sim 8\%$ probability, which is not particularly unlikely and is consistent with our χ^2 statistics.

2.3 BAO Measurements

Measurements of baryon acoustic oscillations (BAO) in galaxy surveys probe the expansion history of the universe and provide evidence for dark energy, independent of supernovae Ia. Before last scattering, the baryons were coupled to the photons. Therefore, initial acoustic perturbations in the density of baryon-photon plasma propagated with the speed of sound. However, since dark matter was cold, the same initial perturbations in dark matter did not propagate. After last scattering, baryon acoustic perturbations also stopped propagating, but (over time) left a gravitational imprint on dark matter, as baryons would have comprised 16% of the density of the universe. As a result, dark matter (and resulting galaxy) distributions contain a characteristic structure (captured in correlation functions) on the scale of the sound horizon at last scattering, r_d. This structure provides a standard comoving ruler that is independent of redshift or orientation. Measuring large scale structure modes perpendicular to the line of sight gives angular diameter distance, D_A, and measurements along the line of sight determine $D_H(z) = \frac{c}{H(z)}$. Combining all modes to suppress noise gives D_v,

$$D_v(z) = \left(z(1+z)^2 D_H(z) D_A(z)^2\right)^{1/3} = \left(z D_H(z) D_c(z)^2\right)^{1/3}, \tag{2.18}$$

where $D_c(z)$ is the co-moving distance. Assuming FRW flat universe $D_c(z) = \int_0^z \frac{c}{H(z)} dz$. In most BAO analysis a fiducial cosmological model is used to assign flux pairs separated in

angle and wavelength to comoving distance and to determine the position of the observed peak. The sound horizon, r_d is constrained by the locations of the acoustic peaks (and not by their heights). The locations of the peaks are determined by pre-recombination physics. Dark energy is negligible at pre-recombination epoch for the fiducial models that are used. In everpresent Λ model, dark energy is not negligible in general at this epoch though the dark energy histories that give a good fit to the data have Ω_{de} close to zero close to recombination. It is possible that using a fiducial model with dark energy not negligible at pre-recombination could yield somewhat different BAO distance measurements.

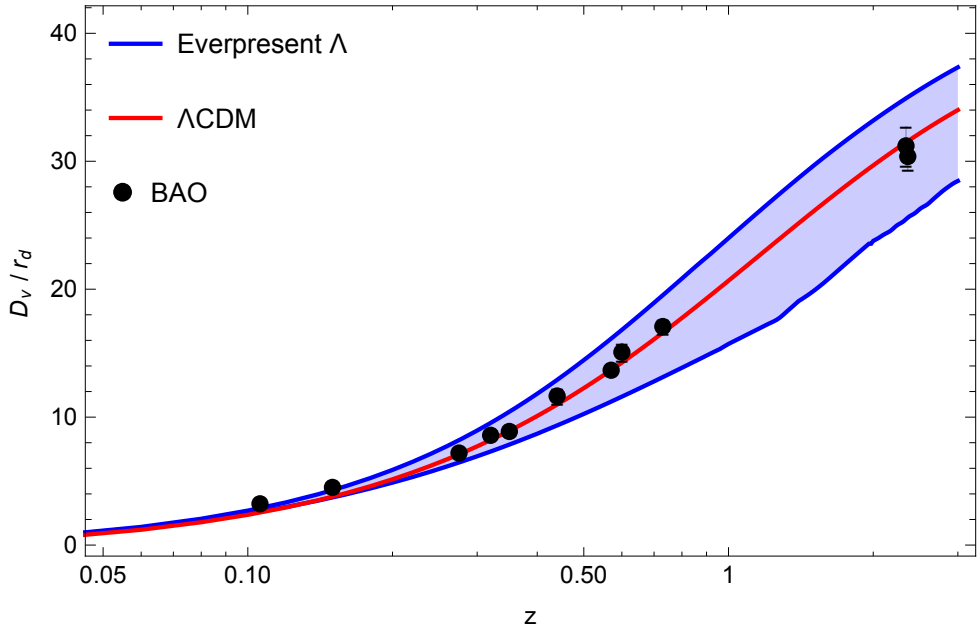

Figure 2.4: BAO measurements from Table 2.3 and model predictions. ΛCDM is in red, while gray is 68% region from everpresent Λ with dark energy histories that give a relatively good fit to the CMB.

Figure 2.4 shows different BAO measurements from Table 2.3, along with everpresent Λ and ΛCDM predictions (using cosmological parameters in Table 2.1).

The dark energy history in everpresent Λ that is a good fit to Planck 2015 CMB data fit well into BOSS [1] bounds as show in Figure 2.5. Fixing the cosmological parameters to best fit values in Table 2.1, there is a 78% chance that Ω_{de} is negative in the range $1.5 < z < 3$. This is indeed consistent with the negative Ω_{de} measured in in Aubourg *et al.* [1] (Figure 2.5), and is in 2.5σ tension with ΛCDM.

	z	Distance(Mpc)		z	Distance(Mpc)
6dF (D_v) [35]	0.106	457 ± 27	SDSS DR9 LRG (D_A)[36]	0.57	1386 ± 45
SDSS DR7 (D_v) [37]	0.15	664 ± 25	WiggleZ (D_v) [38]	0.6	2221 ± 101
SDSS DR7+2dF (D_v) [39]	0.275	1059 ± 27	WiggleZ (D_v) [38]	0.73	2516 ± 86
SDSS DR11 (D_v) [40]	0.32	1264 ± 25	Lyα auto-corr (D_A) [27]	2.34	1662 ± 96
SDSS DR7 LRG (D_v) [41]	0.35	1308 ± 25	Lyα auto-corr (D_H) [26]	2.36	226 ± 8
WiggleZ (D_v) [38]	0.44	1716 ± 83	Lyα auto-corr (D_A) [26]	2.36	1590±60

Table 2.3: BAO data: Volume weighted distance D_v for different z from several sky surveys.

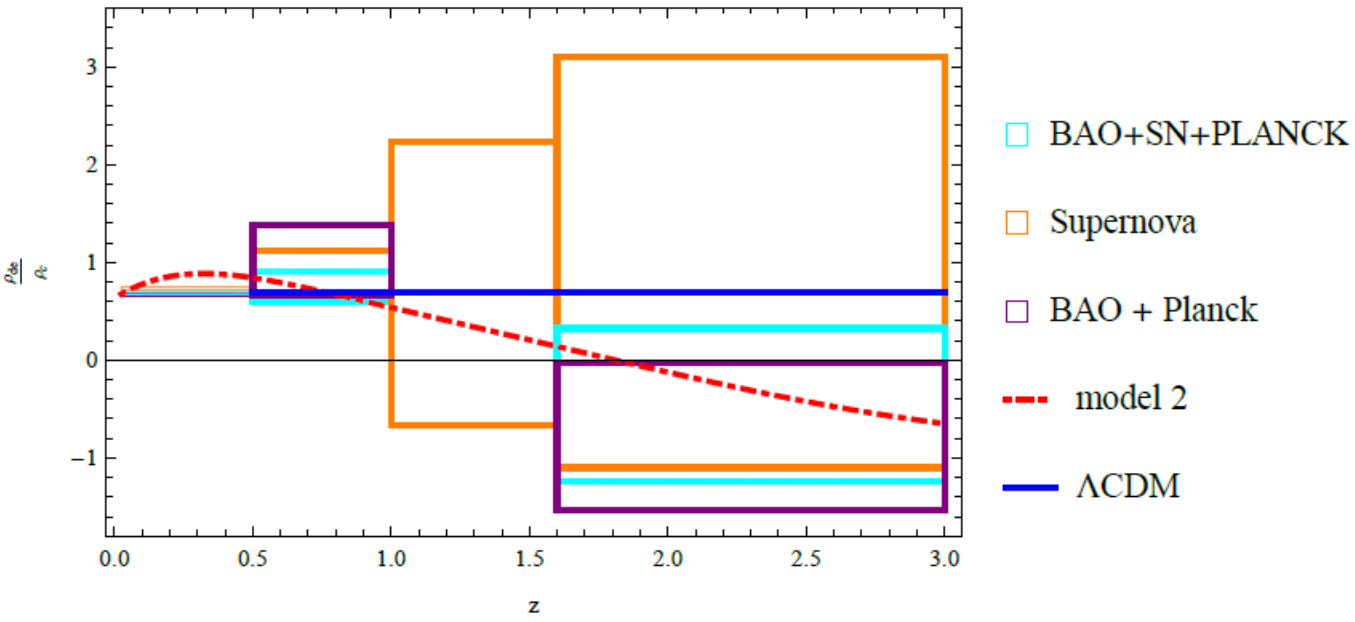

Figure 2.5: Ω_{de} for the different models with BOSS bounds [1].

2.4 Ultramassive Black Holes at High Redshifts

There is overwhelming observational evidence that centers of all large galaxies host supermassive black holes which grow through accretion of surrounding gas. The most efficient phase of this growth leads to bright active galactic nuclei, known a quasars, at luminosities close to the astrophysical upper limit for Eddington accretion. However, quasars at $z \sim 6$ to 7 appear to host black holes more massive than is allowed by Eddington accretion in ΛCDM cosmology, starting from seeds of stellar mass ~ 5 to 20 $M_\odot$, *assuming that they are maximally rotating*. Exotic astrophysical processes may induce super-Eddington accretion rate allowing the quasars to accumulate mass faster, or allow for direct collapse to much more massive black hole seeds. However, it is also possible (e.g. [28]) that the solution may come from revising ΛCDM cosmology so as to allow more time for accretion. Indeed, everpresent Λ produces a range of expansion histories, some of which give the quasars more time to accumulate mass. Blackhole mass is given by [42]

$$M(t) = M_{\text{seed}} \exp\left(\frac{t}{\eta\tau}\right), \tag{2.19}$$

where M_{seed}, the mass of the seed is assumed to be $20M_\odot$, η is the accretion efficiency, t is the age of the quasar and $\tau = \frac{Mc^2}{L_{Edd}}$ is given by

$$\tau = \frac{\sigma_T c X}{4\pi G m_p} \tag{2.20}$$

with σ_T being Thomson scattering cross-section, c is the speed of light, G is the gravitational constant, m_p is the mass is a proton and $X = (1 + 0.75)/2$ assumes Helium mass fraction of 25%. The accretion efficiency depends on the spin of the blackholes [42]:

$$\epsilon = \frac{\eta}{1-\eta} = \frac{1}{\epsilon_g}\left(1 - \sqrt{1 - \frac{2GM}{c^2 r_{\text{ISCO}}}}\right) \tag{2.21}$$

$$r_{ISCO} = \frac{GM}{c^2}\left(3 + \alpha_2 - \sqrt{(3-\alpha_1)(3+\alpha_1+2\alpha_2)}\right) \tag{2.22}$$

$$\alpha_1 = 1 + (1-a_*^2)^{1/3}\left((1+a_*)^{1/3} + (1-a_*)^{1/3}\right) \tag{2.23}$$

$$\alpha_2 = \sqrt{3a_*^2 + \alpha_1^2} \tag{2.24}$$

where a_* is a dimensionless spin parameter.

Considering two quasars J010013.02+280225.8[43] and J338.2298+29.5089[44] at redshift 6.30 and 6.658 respectively Figure 2.6 shows the accretion efficiency and spin parameter of the blackholes the host. The black holes cannot be maximally spinning $a_* = 1$ in

either ΛCDM and Everpresent Λ, though Everpresent Λ does allow for higher and similar spins/efficiencies.

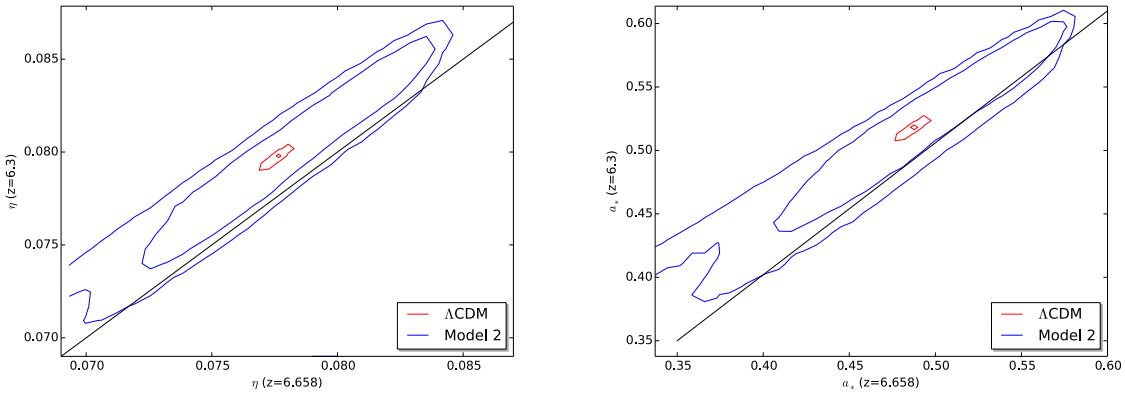

Figure 2.6: 68% and 95% constraints on accretion efficiency η and spin parameter a_* of two quasar blackholes in ΛCDM and Everpresent Λ (Model 2). For both models the two blackholes cannot maximally spinning that is, $a_* \neq 1$, even though everpresent Λ allows for a much bigger range.

2.5 Primordial Lithium-7

Big Bang Nucleosynthesis (BBN) predicts the abundance of light cosmological elements (D, ^{3}He, ^{4}He,^{7}Li) that are produced the first 10 seconds to 20 minutes after the Big Bang, when the universe was still hot and dense. Astronomically observed abundances of Deuterium and Helium-4 are in agreement with BBN predictions, while predicted Helium-3 is within the observed bounds. However, for Lithium-7, three times more abundance is predicted than is observed, which is known as the *Lithium problem*.

Fields [45] discusses a number of possible solutions to this problem. One solution might be that the observed Lithium-7 in the halo stars is not the initial abundance but some of the Lithium-7 was destroyed through nuclear binding. For some stars Lithium destruction has been studied, some groups [46] have found some Lithium depletion. Though this might be a direction towards the solution to the Lithium problem, it is far from clear since in metal-poor stars (where we expect to have less Lithium-7 depletion) Lithium-7 abundance is nowhere near the predicted value.

	Observation	Everpresent Λ	ΛCDM
D/H ($\times 10^{-5}$)	2.547 ± 0.033	2.64	$2.584^{+0.036}_{-0.035}$
^{3}He/H ($\times 10^{-5}$)	1.1 ± 0.2	1.09	$1.026^{+0.005}_{-0.006}$
^{4}He/H	0.249 ± 0.009	0.2311	0.248 ± 0.001
^{7}Li/H ($\times 10^{-10}$)	$1.23^{+0.34}_{-0.16}$	3.583	4.507 ± 0.08
χ^2		57	89

Table 2.4: Primordial light cosmological elements predictions from BBN with different Cosmologies. The uncertainties in ΛCDM come from uncertainties in baryon density.

The problem might be in the nuclear physics, the BBN calculations might be leaving out some reactions or have incorrect rates, but few reactions have been found to be relevant for producing light elements and these have been studied in the laboratory. Another, solution might be that dark matter introduces new processes that can alter light elements during BBN or after BBN [47].

Everpresent Λ changes the cosmology, the expansion of the universe is governed by

$$H^2 = \frac{8\pi}{3} G \left(\rho + \Lambda(t)\right). \tag{2.25}$$

We run Timmes's BBN code [48] using (N_{eff}, η) from Planck 2015. η is the photon-baryon ratio

$$\eta_b = 2.7377 \times 10^{-8} \Omega_b h^2 \tag{2.26}$$

which depends on[1] $\Omega_b h^2$. For ΛCDM we take $N_{\text{eff}} = 3.00$ and $\Omega_b h^2$ in Table 2.1. For Everpresent Λ we take $N_{\text{eff}} = 3.00$ and sample $\Omega_b h^2$ from chains with dark energy histories that have relatively good χ^2 in CMB data.

Deuterium is measured by observing the absorption of hydrogen in quasar spectra. Several groups have measured D/H abundance from different quasars at different redshifts. The highest bound for D/H is given by Burles and Tytler [49] D/H $=3.39 \pm 0.3 \times 10^{-5}$ and lowest bound Kirkman *et al.* [50] D/H $= 2.42^{+0.35}_{-0.25} \times 10^{-5}$ measured from light from quasar 1009+2956 at z=2.504. In Table 2.4 measurements with the lowest uncertainties from Cooke *et al.* [51] are used. Bania *et al.* [52] determined primordial Helium-3 abundance in the Milky way setting the highest bound to be ^{3}He/H $= 1.1 \pm 0.2 \times 10^{-5}$. Astronomical observations of metal poor halo stars[53, 54, 55] give relative primordial abundance of

[1] h is dimensionless Hubble parameter, h = Hubble Parameter/(100km s^{-1}Mpc^{-1}).

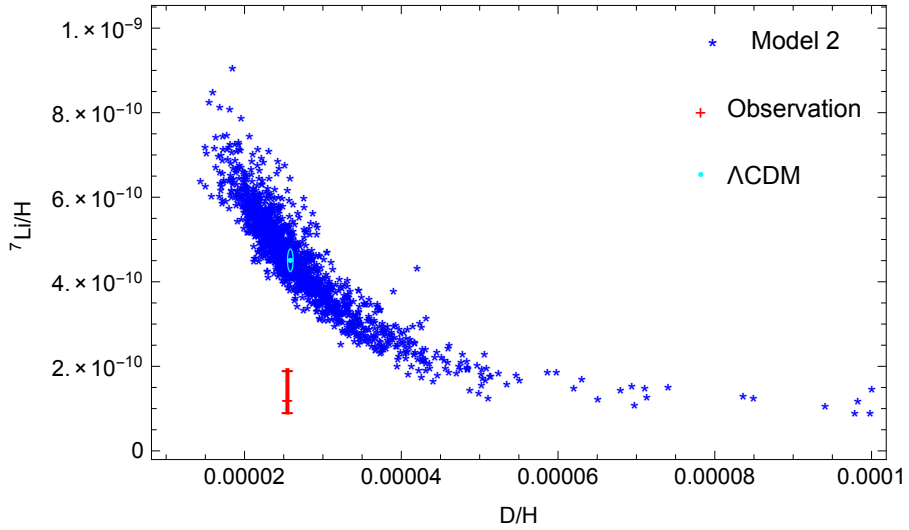

Figure 2.7: Deuterium vs Lithium-7 abundance predicted by everpresent Λ and ΛCDM. For everpresent Λ, when less Lithium-7 is produced there is more Deuterium.

$^7\text{Li/H} = 1.23^{+0.34}_{-0.16} \times 10^{-10}$. Olive *et al.* [56] determined primordial Helium-4 abundance to be $^4\text{He/H} = 0.249 \pm 0.009$.

For everpresent Λ, fixing the value of η_b, different dark energy histories predict different abundances for the elements. Histories of dark energy that correctly predict Lithium-7 predict a higher abundance of Deuterium than the highest observed bound. While the best fit everpresent Λ model is not very good, it is still preferred to ΛCDM. When varying N_{eff} between 2.3 and 3.5, the Lithium-7 abundance decreases as N_{eff} decreases as shown in Figure 2.9. While the abundance of Deuterium increases as N_{eff} decreases. Varying the value of N_{eff} for the same history of dark energy will not solve the Lithium-7 problem without creating a Deuterium problem.

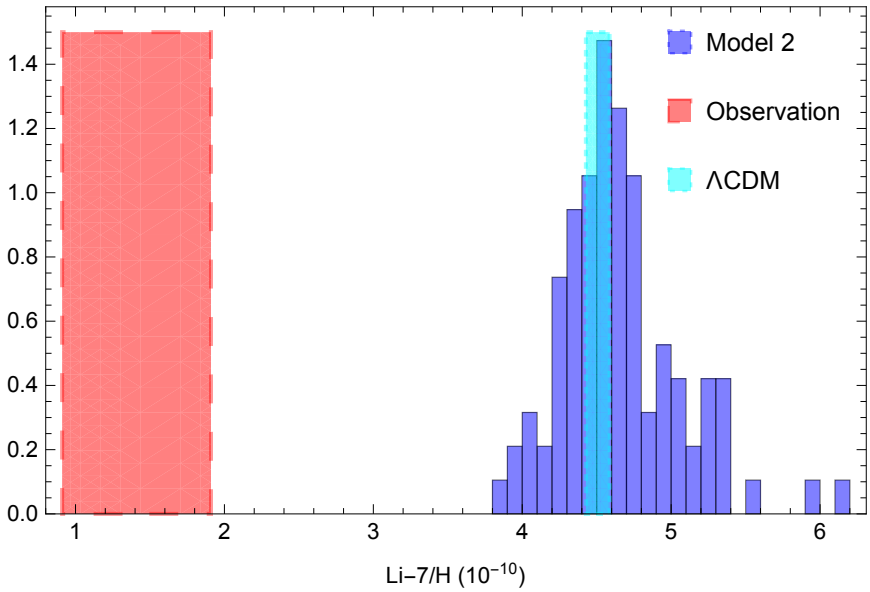

Figure 2.8: Shows that model 2 dark energy histories that give the Deuterium abundance have higher Lithium-7 abundance than observed. Blue region is the probability distribution of Lithium-7 abundance given that Deuterium abundance is 2.547 ± 0.033 in model 2, red region is observed Lithium-7 abundance and cyan region is Lithium-7 abundance in ΛCDM.

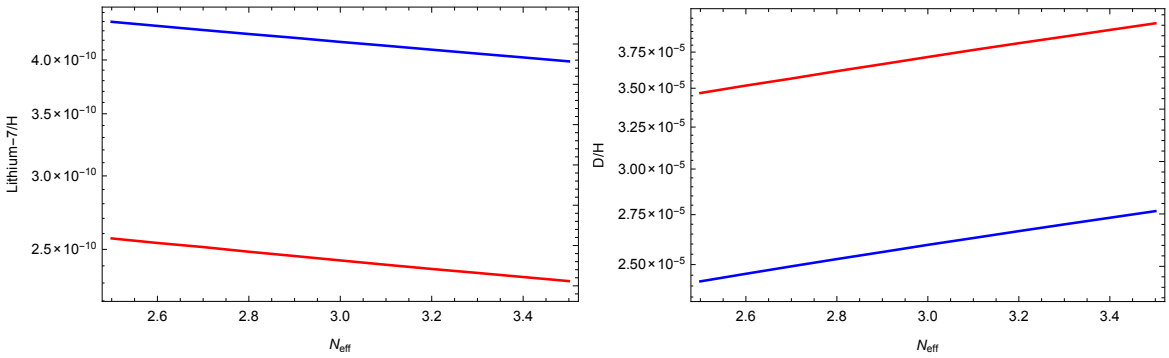

Figure 2.9: Plot of Deuterium abundance vs N_{eff} and Lithium-7 abundance vs N_{eff} predicted by two different dark energy histories showing that varying the value of N_{eff} for the same history of dark energy will not solve the Lithium-7 problem without creating a Deuterium problem.

Chapter 3

Non-locality Effects on Wave and Particle Propagation

The causal set hypothesis makes a definite statement that the fundamental structure of a spacetime manifold is discrete and Lorentz invariant. Finding signatures of Lorentz invariant discreteness at low energy scales would be interesting for theories with this assumption. An experiment violating Lorentz invariance will disfavor such theories. As of date high-energy observations from the Fermi Large Area Telescope(LAT) of gamma-ray burst GRB090510 are the most constraining sources for stochastic Lorentz invariant violation, setting the bound on energy $> 2.8E_{pl}$ [3].Since the underlying discreteness is Lorentz invariant, because the causal elements are assumed to be Poisson distributed as discussed in Chapter 1, this induces fluctuations in the worldline of a massive particle travelling on the causal set. In this chapter we study the effects of such fluctuations on particles propagating on a causal set which was first introduced by Dowker *et al.*[14, 57, 58]. The worldline fluctuations are modelled as diffusion of a point particle (or wave) with the causal set as a bath. This diffusion induces statistical energy gain which can be detectable by astronomical observations if the particle travels over cosmic distances. Observed cosmic dust sets bounds on the diffusion constant. The diffusion constant depends on the non-locality scale of the model, so bounds set on the diffusion constant in turn set bounds on the non-locality scale.

Another way in which swerves maybe be observed is fuzziness of a distant source. This is because the particles will not travel on a exact geodesics, hence there will be a spread in the possibility of the positions of the source. This might observed by a detector with high sensitivity.

3.1 Propagation of massive particles in discrete spacetime

A massive paricle propagating in a causal set will not travel in an exact geodesics, since the discretization is not regular. The particle will have to swerve when moving from one element of the causal set e_i to another e_j. We assume that it will try to stay in a straight line as much as possible. The process at macroscopic scale, after many steps of the random walk can be described approximately by a diffusion process. The diffusion is on a phase space $\mathbb{H}^3 \times \mathbb{M}^4$, where $\mathbb{H}^3$ is the mass shell (Lobachevsky space) and $\mathbb{M}^4$ is Minkowski spacetime. The diffusion in spacetime is driven by the diffusion of momentum in the mass shell. Philpott *et. al*[58] showed if the underlying process for particle propagation is Lorentz and translation invariant, it will always give rise to the diffusion equation[1]

$$\frac{\partial \rho}{\partial \tau} = k\nabla^2 \rho - \frac{1}{m} p^\mu \frac{\partial}{\partial x^\mu} \rho, \tag{3.1}$$

where $\rho \equiv \rho(p^\mu, x^\mu; \tau)$ is a scalar distribution on $\mathbb{H}^3 \times \mathbb{M}^4$, ∇^2 is the Laplacian on $\mathbb{H}^3$, m is the mass of the particle and k is the diffusion constant,that will depend on the forgetting time or number. Equation (3.1) is not suitable to compare with experiments or observations since it is in terms of proper time. It can be rewritten in terms of cosmic time

$$\frac{\partial \rho}{\partial t} = \frac{-p}{\sqrt{1 + (p/m)^2}} \frac{\partial \rho}{\partial x} + k \frac{\partial}{\partial p} \left(\frac{\partial}{\partial p} \left(\frac{\rho}{\sqrt{1 + (p/m)^2}} \right) \right), \tag{3.2}$$

where $\rho \equiv \rho(p^\mu, x^\mu; t)$. The change in momentum is small at each step but it may add up as the number of steps increases.

Dimension analysis show that the diffusion constant is proportional to the square of the mass of the particle,

$$k \propto m^2.$$

To get the dependency of the diffusion constant on the discretization scale and the forgetting time (or forgetting number) simulation of the models was done. We generate a causal set by sprinkling points on a Minkowski manifold. We then let the particle propagate on the generated causal set using the set of rules specified in each model.

[1] $c = k_B = 1$

3.1.1 Point Particle Models

If the process of a massive particle propagation in a causal set is a Markovian process and is also Lorentz and translation invariant then it can be modelled by the diffusion equation (3.1). In these models the particle will try to stay in a straight line as much as possible. In order for the particle to minimize change in direction, it is given a short memory that lasts for a period $\tau_f(n_f)$ called the forgetting time (forgetting number), which is associated with the non-locality scale. The longer the memory the closer its trajectory will be to a geodesic. We consider two models discussed in Reference[58]:

Model 1a: Given a segment of the path of the particle $e_1, \ldots, e_{n-1}, e_n$ the next element e_{n+1} is selected such that it is in the causal future of e_n and satisfies the following conditions:

$$\begin{aligned} d(e_{n-1}, e_{n+1}) &\leq 2n_f, \\ d(e_n, e_{n+1}) &\leq n_f(\text{ Maximum } d(e_n, e_{n+1})) \end{aligned}$$

where $d(e_i, e_j)$ is the number of links between e_i and e_j, assuming $e_i \prec e_j$. There will be lot of elements in C that will satisfy these conditions. e_{n+1} is then chosen randomly from these elements. Only n_f elements in the particle's past are relevant in choosing e_{n+1}, as shown in Figure 3.1a.

Model 1b: Given a segment of the path of the particle $e_1, \ldots, e_{n-1}, e_n$ the next element e_{n+1} is selected such that it is in the causal future of e_n and

$$d(e_{n-n_f}, e_{n+1}) = n_f, \quad \text{or minimize if can not meet} n_f$$

Again there will be lot of elements in C satisfy these conditions. e_{n+1} is chosen randomly from these elements. Again only n_f of the elements in particles past are relevant.

The forgetting number n_f is chosen such that $1 \ll n_f \ll n_{macro}$. $n_f \gg 1$ so that the swerve is minimal, that is the particles deviation from exact geodesic is small. It must also be much less than n_{macro} so that the process is approximately Markovian.

Model 2: Consider a particle starting from an element e_n and momentum p_n the next element e_{n+1} is chosen such that, e_{n+1} is in the causal future of e_n and within the forgetting time, τ_f and $|p_n - p_{n+1}|$ is minimized as shown in figure 3.1b. This model is not intrinsic to causal sets as it uses forgetting time τ_f, but it is easier to simulate than the intrinsic models.

In the simulations a causal set is generated by sprinkling in Minkowski spacetime, and the first two elements in the path of the point particle were added by hand so that the

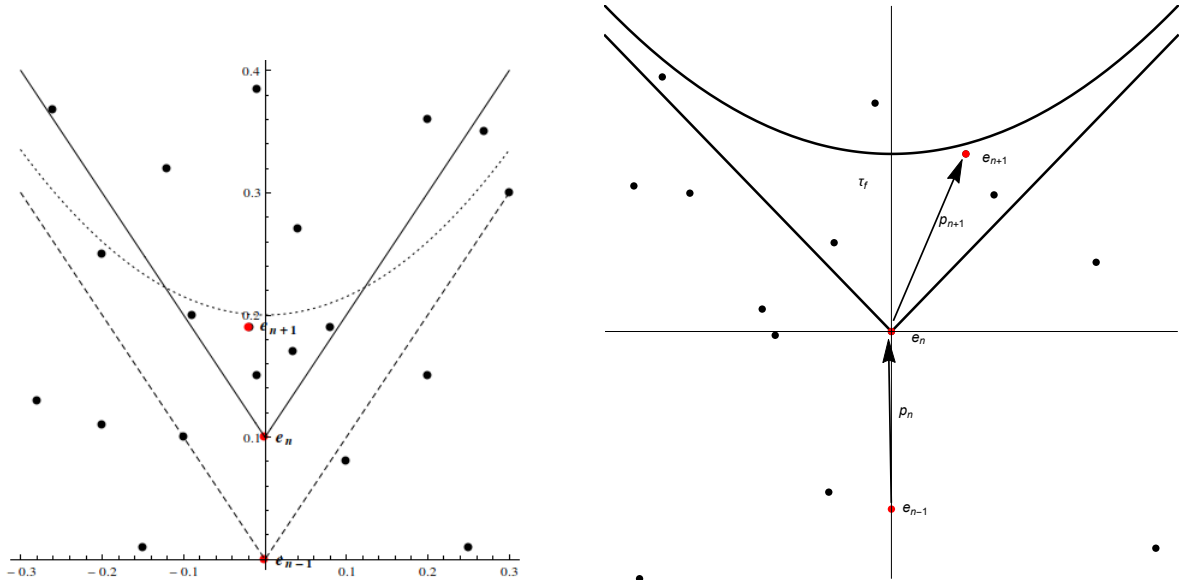

(a) Model 1(a)

(b) Model 2

Figure 3.1: (a)Propagation of a point particle (red dots) using model 1(a). (b)Propagation of a particle from e_n to e_{n+1}, e_{n+1} is selected such that it is within the causal future of e_n and within the forgetting time (that is, below the parabola). The vector e_n to e_{n+1} is chosen such that it is as vertical as possible, so that the change in momentum is minimal.

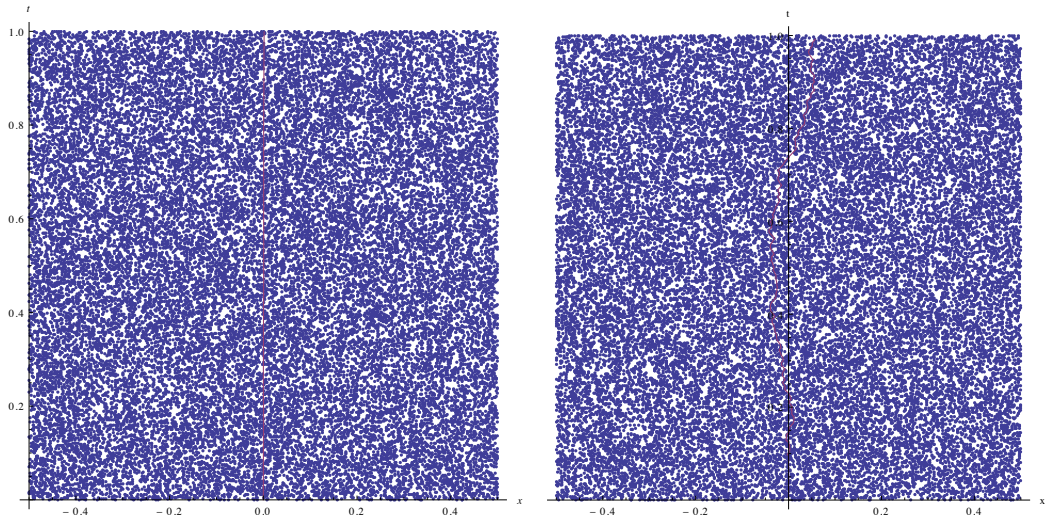

(a) Model 2, N=34 178, $\tau_f = 0.1$ (b) Model 1(b),N=34 089, $n_f = 20$

Figure 3.2: Propagation of a particle for the two models.

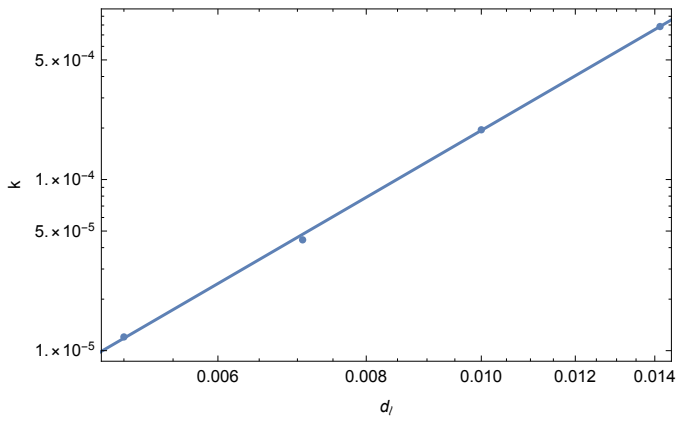

Figure 3.3: Plot of diffussion conastant k vs discretization scale d_ℓ, with the best fit $4.04\log(d_\ell) + 10.05$.

particle starts with zero momentum. Then the next element is chosen using the set of rules for each model.

For each $\tau_f's$ between $\tau_f = 0.04$ and $\tau_f = 0.15$, 500 trajectories were simulated. Each trajectory ran from $\tau = 0$ to $\tau = 1$ and was simulated on a new sprinkling and the momentum at $\tau_f = 0.95$ was recorded together with the end position of the particle. Then for each τ_f, the frequency of momentum and position was then fitted to equation (3.2) to obtain the value of k and the results are shown in Figure 3.4, $\tau \propto \tau_f^{-5}$ for both 2D and 3D.

Using model 1(a) for each n_f between $n_f = 8$ and $n_f = 20$, 500 trajectories were simulated. Again the position and momentum were recorded when $d(e_1, e_i) = 172$. Using the same technique as done in model 2, the value of k for each n_f was calculated and the results are shown in Figure 3.4. Some of the trajectories propagated to the boundary and bounced back at the next step. These trajectories were not included.

The k dependence on the discretization scale was obtained through fitting the distribution of momentum and position frequency to equation (3.2) for different d_ℓ's, $N = \{32\,768, 20\,000, 10\,000, 5\,000\}$ and the results are shown in Figure 3.3, $k \propto d_\ell^4$. These results agree with Philpott's [16].

$$k \sim \frac{m^2 d_\ell^4}{\tau_f^5}. \tag{3.3}$$

In the next section, we discuss the possibilities that the effects of the swerves maybe observed in a laboratory or in astrophysics. If none of these effects have been observed, then the observational data sets limits on the diffusion constant k.

3.1.2 Bounds on Diffusion Constant

Lots of work has been done in setting bounds on the diffusion constant by Dowker *et al.*[14] and Kaloper *et al.*[15]. When considering non-relativistic particles, equation (3.2) can be approximated by

$$\frac{\partial \rho}{\partial t} = k \nabla^2 \rho, \tag{3.4}$$

and has the solution

$$\rho = A(t) \exp\left(-\frac{p^2}{4kt}\right), \tag{3.5}$$

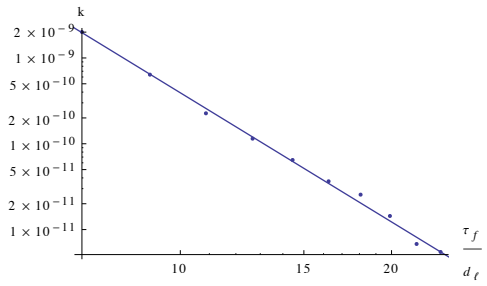

(a) 1 + 1 D model2

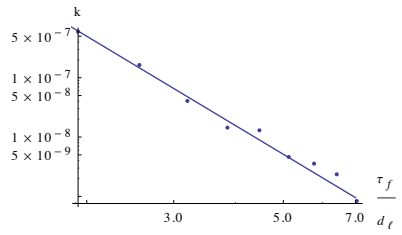

(b) 2 + 1 D model2

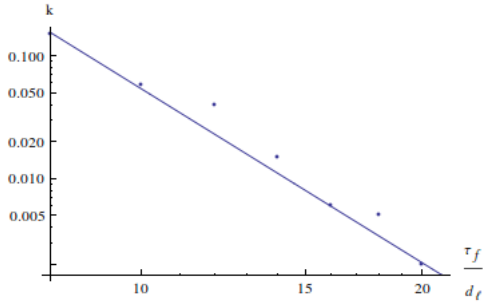

(c) 1 + 1 D Model1(a)

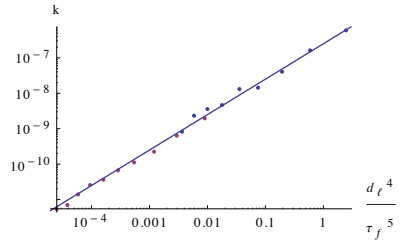

(d) model2

Figure 3.4: This plot shows the relationship between forgetting time τ_f and the diffusion constant k. (a) for 1+1D the best fit is $k = 3.9 \times 10^{-5} \left(\frac{t_f}{d_\ell}\right)^{-5}$ and (b) for 2+1D the best fit is $k = 1.6 \times 10^{-5} \left(\frac{t_f}{d_\ell}\right)^{-5}$. (c) 1 + 1D model 1(a) the best fit is$2708.46 n_f^{4.709}$ (d)For 1+1D $\left(\frac{d_\ell^4}{\tau_f^5}\right)$ vs k and 2+1D model $\left(\frac{d_\ell^4}{\tau_f^5}\right)$ vs 2.5k

which is in the form of Maxwell's distribution of non-relativistic gas at temperature T,

$$\rho = A(t) \exp\left(-\frac{p^2}{2mk_BT}\right). \tag{3.6}$$

These two equations (3.5) and (3.6) lead to

$$k = \frac{\Delta T}{\Delta t}\frac{mk_B}{2}, \tag{3.7}$$

where ΔT is change in temperature and Δt is change in time. If the value of k is large, the swerves will accelerate hydrogen gas in a lab causing it to spontaneously heat up in a short time. Since this has not been observed this sets a bound on the value of k. Dowker *et. al*[14] assumed that the minimum change in temperature of the hydrogen gas that could be detected in the laboratory was a heat by a millionth of a degree per second, then

$$k \lesssim \frac{\Delta T}{\Delta t}\frac{mk_B}{2} \tag{3.8}$$

$$\lesssim 10^{-44} GeV^3. \tag{3.9}$$

Equation (3.8) shows that heavy particles gain less energy due to swerves and the energy gained increases over time. Using this bound for hydrogen gas, the forgetting time,

$$\tau_f = \left(\frac{2m^2 d_{pl}^4}{k}\right)^{1/5}$$
$$\simeq 2 \times 10^{10} \ell_p.$$

Kaloper *et. al*[15] with the hope that very old particles would set better bound on the value of k, considered very old and cold astrophysics molecular cloud, Edge Cloud 2 in our galaxy. This cloud is composed of NH_3. They considered the age of NH_3 in Edge Cloud 2 to be the age of Milky Way and that its average kinetic temperature is $T \approx 20K$ and $m = 17GeV$. Assuming that the cloud also loses energy through blackbody radiation, they set the bound on $k \lesssim 10^{-41} GeV^3$.

Cosmic neutrinos were expected to set a tighter bound on the value of the diffusion constant because they are light ($m \approx 0.01eV$) and electromagnetically neutral so they are expected to have negligible energy losses. Kaloper *et. al*[15] considered cosmic neutrinos being accelerated by the swerves such that they behave as hot dark matter contradicting the assumption that dark matter should be cold. This set the bound $k \lesssim 10^{-61} Gev^3$.

Experiment	bound on k	τ_f (in units of ℓ_p)
Laboratory hydrogen	$k \lesssim 10^{-44} GeV^3$	2×10^{10}
NH_3 in Edge Cloud 2	$k \lesssim 10^{-41} GeV^3$	6×10^9
Cosmic neutrino	$k \lesssim 10^{-61} GeV^3$	6×10^{13}

Table 3.1: Bounds of non-locality scale

Origin of high energy cosmic ray is not known. If the comic rays are protons they could only have been produced less than 20 Mpc away, if they were produced any further they would have decayed through photo-pion production in collisions with the CMB photons. There are suggestions that these high energy cosmic rays result from Supernovae explosions, pulsars, active galactic nuclei, e.t.c. For swerves to be mechanism responsible for high energy cosmic ray the swerves will have to accelerate the protons to gain $250MeV$. The time it will take for a protons to travel from $20Mpc$ to us will approximately be 2 hours. The bounds on energy gain set by NH_3 in Edge Cloud 2 would be,

$$\begin{aligned} \langle \Delta E \rangle &= \frac{3k}{2m} \Delta t \\ &\lesssim (4.3 \times 10^{-14} eV\, s^{-1})(7200s) \\ &\lesssim 3.1 \times 10^{-10} eV. \end{aligned} \tag{3.10}$$

Unfortunately swerves can not be responsible for the high energy cosmic rays. At least not the simple model of swerves, but maybe if k depended on local factors like the particle density and temperature.

3.2 Propagation of massless particle

Unlike in the massive case, a massless particle will only have diffusion in the magnitude of momentum but not the direction. At present there is no existing model of massless particles propagating in discrete Lorentz invariant spacetime (causal set). Considering an element p, the probability that there is an element q in the future light cone of p will be close to zero. When one tries to use models like the ones for the massive case, the final trajectory will not approximate a geodesic as in the case of a massive particle. Though a model for massless particles has not yet been formulated as in the case of massive particles, but as long as the underlying model is Lorentz- and translation invariant, Philpott *et. al*[59] showed that for a process that undergoes stochastic evolution on a manifold of states, M,

in some spacetime parameter t, can be described by a current J and a continuity equation,

$$J^A = -\partial_B \left(K^{AB}\rho\right) + v^A\rho \tag{3.11}$$

$$\frac{\partial\rho}{\partial t} = -\partial_A J^A \tag{3.12}$$

where $\rho = \rho(x^\mu, p^a, t)$ the probability distribution is a scalar on $\mathbb{M}^4 \times \mathbb{H}^3_0$ which leads to the diffusion equation,

$$\frac{\partial\rho}{\partial t} = -\frac{p^i}{E}\partial_i\rho - (k_1 + k_2)\frac{\partial\rho}{\partial E} + k_1 E\frac{\partial^2\rho}{\partial E^2}. \tag{3.13}$$

for a non-expanding universe. This suggest that swerves will induce fluctuations in the magnitude of momentum but not the direction of the particle. The diffusion constant k_1 causes a spread in the momentum distribution. There is also a drift in the spectrum, to lower energies or higher energies depending on the sign of k_2. In an expanding universe the photons will be red-shifted and these effects can be incorporated in the v^A term in equation (3.11), $\Delta v^E = dE/dt = -E\dot{a}/a$, hence

$$\frac{\partial\rho}{\partial t} = -\frac{p^i}{E}\partial_i\rho_t - (k_1 + k_2)\frac{\partial\rho}{\partial E} + k_1 E\frac{\partial^2\rho}{\partial E^2} + \frac{\dot{a}}{a}\frac{\partial}{\partial E}(\rho E). \tag{3.14}$$

3.2.1 Bounds on k_1 and k_2

To set bounds on the value of k_1 and k_2 the CMB photons seem to be ideal. This is because these have travelled for a long time hence have experienced the swerves for a long time. The CMB is also a good candidate for setting the bounds since the spectrum has been determined to a great precision. Since the swerves are expected to spread and shift the energy distribution, the fact that the CMB spectrum have travelled so far but remain so perfectly thermal sets bounds on the value of k_1 and k_2.

Philpott *et. al*[14] placed constraints on k_1 and k_2 by numerically evolving an initially blackbody spectrum at a temperature of $2.728K$ according to equation (3.13) for a range of values of k_1 and k_2 from last scattering to today for a non-expanding universe. To get a concrete bound on k_1, they set $k_2 = 0$ and did the same for k_2, the bounds they found were

$$k_1 < 3 \times 10^{-44} kg\, m^2 s^{-3} \tag{3.15}$$

$$-1 \times 10^{-43} < k_2 < 1 \times 10^{-43} kg\, m^2 s^{-3} \tag{3.16}$$

3.2.2 Propagation of waves

The models for swerves assumes a particle to be a point size, jumping from one causal element to another, but all known particles are larger than a causal element, if a causal element is of the order of plank scale. In this section we model a particle as a wave packet propagating in a causal set. For this we use causal set D'Alembert operator, denoted as B_ϵ. This operator was first introduced by Sorkin[60]. It is an analog of D'Alembert operator, $\Box := -\frac{\partial^2}{\partial t^2} + \frac{\partial^2}{\partial x^2}$.

$$B\phi(x) = \frac{4}{\ell_p^2}\left(-\frac{1}{2}\phi(x) + \sum_{\substack{y\in C\\ y\prec x}} f(n(x,y))\phi(y)\right), \tag{3.17}$$

with,

$$f_\epsilon(n) = \begin{cases} 1 & \text{if n=0} \\ -2 & \text{if n=1} \\ 1 & \text{if n=2} \\ 0 & \text{otherwise.} \end{cases} \tag{3.18}$$

The causal set D'Alembert operator is non-local. $B_\epsilon\phi(x)$ as shown in equation (3.17), is a sum of $\phi(y)$'s, the value of the field at point y, in the past of x with each term weighted differently. The weight depends on the spacetime distance between x and y. Recall that a causal set has no metric, neighbours of a causal element x are causal elements that have no elements in the causal interval $n(x,y) := \text{card}\{z \in C | x \prec z \prec y\}$. When $n(x,y) = 0$, we say that y is in the zeroth layer of x. If $n(x,y) = 1$, then y is in the first layer of x and so on.

For $\mathbb{M}^2$ as discussed in Appendix A, the operator yields,

$$\langle B\phi(x)\rangle = \Box\phi(x) + \text{corrections.} \tag{3.19}$$

Each sprinkling will give a different causal set, resulting in a different sets of $n(x,y)$ for different causal sets resulting in fluctuating $B_\epsilon\phi(x)$. In the simulations several sprinkles are done for each density. The corrections decrease as the density increases, but the fluctuations grow as density grows. The function $f_\epsilon(n)$ in equation 3.20 was then introduced by Sorkin[60] as regulator, to stabilize the fluctuations

$$f_\epsilon(n) = (1-\epsilon)^n\left(1 - \frac{2\epsilon n}{1-\epsilon} + \frac{\epsilon^2 n(n-1)}{2(1-\epsilon)}\right) \quad \text{and} \quad \epsilon = \left(\frac{\ell_p}{\ell_k}\right)^2 \tag{3.20}$$

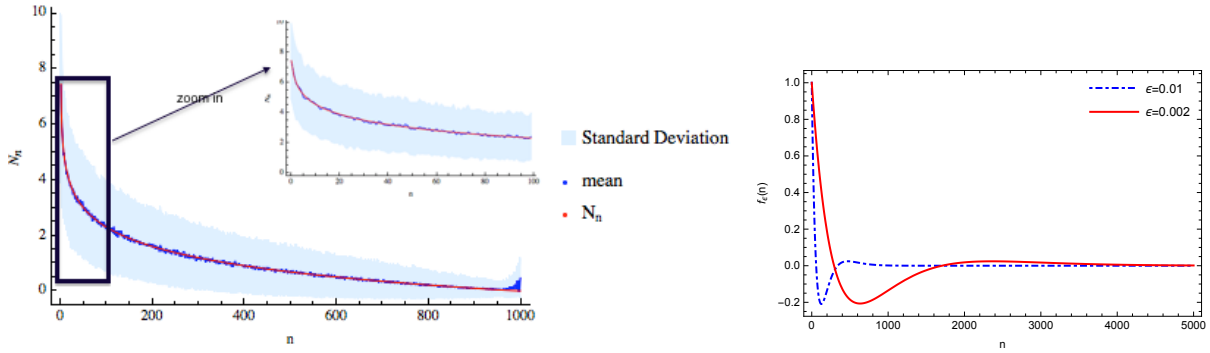

(a) Plot of N_n the number of causal intervals with n elements. (b) Dumping function

Figure 3.5: Damping fluctuations

where ℓ_k is the non-locality scale. The causal set D'Alembert operator can now be written as,

$$B_\epsilon \phi = \frac{4}{\ell_k^2}\left(-\frac{1}{2}\phi(x) + \epsilon \sum_{\substack{y\in C \\ y\prec x}} f_\epsilon(n(x,y))\phi(y)\right). \tag{3.21}$$

Figure 3.5b, shows that if $n(x,y)$ is large then weight of $\phi(y) \sim 0$.

To propagate the wave packet one has to first choose the value of ϵ to use. To do this we used different values of ϵ to calculate the value of ϕ at the top of a 2D flat diamond. The value of $\phi(x)$ is calculated for 100 different causal sets. Figure 3.9 shows that the fluctuations grow as ϵ increases. This is expected because if ϵ is large then only a small portion of the past is used, hence more diffusion. For very small ϵ though the fluctuations are small, the value of the mean is far from the correct value of $\phi(x)$. This is because small ϵ implies large memory and since in this calculation a finite causal set is used most of the past is not available, this leads to errors due to infra-red cut-off. In Appendix A we show one way to account for such errors. For example, $\phi(u,v) = 1$ in a 2D flat causal diamond is a solution of B_ϵ, therefore $B_\epsilon \phi(u,v) = 0$,

$$\phi(x) = 2\ell^{-2}\int du \int dv\, \theta(u)\theta(v)\phi(y) e^{-uv\ell^{-2}}\left(1 - 2\ell^{-2}uv + \frac{\ell^{-4}}{2}(uv)^2\right), \tag{3.22}$$

as show in Appendix B. Figure 3.9 shows that for small ϵ, the cut-off introduced by using a finite causal set generates errors. For analysis it is important to be able to separate

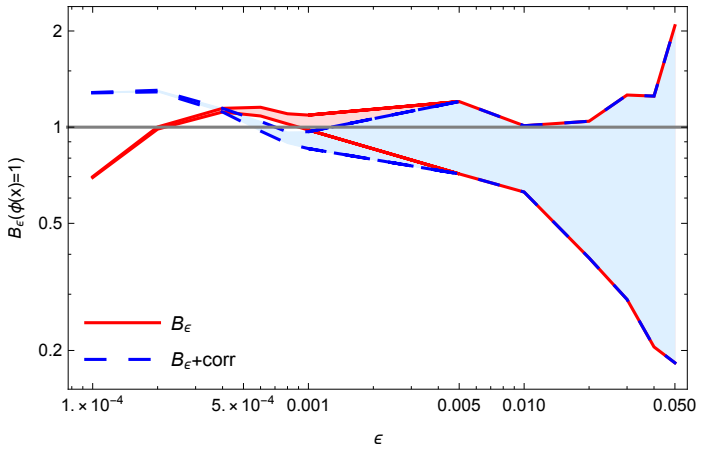

Figure 3.6: Plot of $\phi(u,v) = 1$ vs ϵ for $v = \sqrt{2}/2$ and $u = \sqrt{2}/2$.

deviation from continuum results that is due to errors caused by the infra-red cut-off from deviations due to non-locality of the operator B_ϵ. For $\phi(u,v) = 1$, the error due to the cut-off is

$$\phi(u,v)_{error} = 2\ell^{-2}A\left(\frac{1}{2}e^{-u_0v_0\ell^{-2}}u_0v_0 - \frac{1}{2}e^{-u_0v_0\ell^{-2}}\ell^2\right) \tag{3.23}$$

To check if the fluctuations increase with time we sprinkle a causal set C_n and then add points by hand after the sprinkling which are then used as check point. For example in a diamond as shown in figure 3.7a, the x_i's are the points added in by hand used as checkpoints. We calculated the value of $\phi(x)$ for the x_i's for 100 different causal sets with the same discreteness scale. Figure 3.8 shows the variance of $\phi(x)$ at these points. Fluctuations increase with time.

A causal sets is generated by sprinkling to a 2D causal diamond and initial conditions are set by putting values of the wave packet for causal elements in the red region in figure 3.7a and then propagate the wave packet, $\phi(u,v) = e^{-\frac{(v-0.7)^2}{0.05}}$ using (3.21) for different sprinklings and different ϵ, which gives the results that $k_1 \propto \ell_k^{-2.5}$ and $k_2 \sim 0$. Thus there is no drift in the energy.

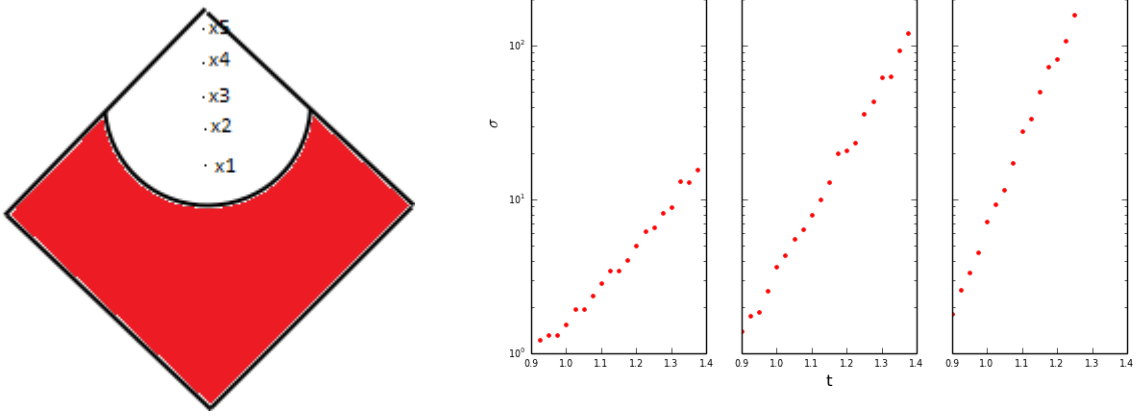

(a) Check Points added by hand.

(b) Fluctuations propagate in time.

Figure 3.7: (a)x's are points added by hand, red region where value of $\phi(x)$ is put in by hand, initial conditions.(b)Shows variance of the fluctuation vs time at points shown in Figure 3.7a.

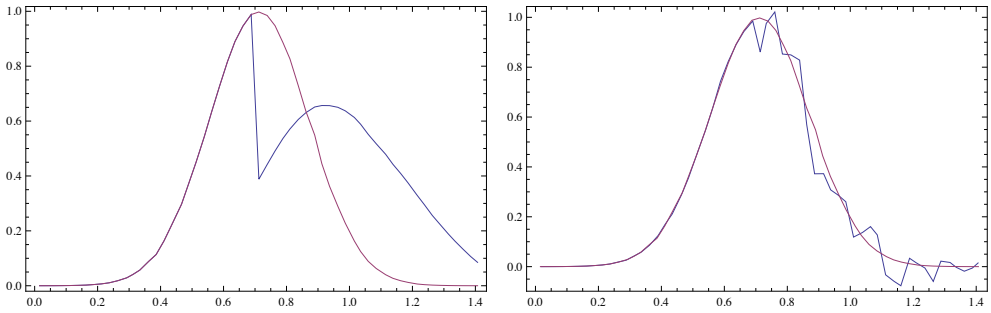

(a) $\epsilon = 0.0001$

(b) $\epsilon = 0.005$

Figure 3.8: t vs $\phi(x)$ for $-0.01 < x < 0.01$ avaraged at each time step. Red plot is the continuum function and blue is the value of $\phi(u, v)$ from a causal set simulation.

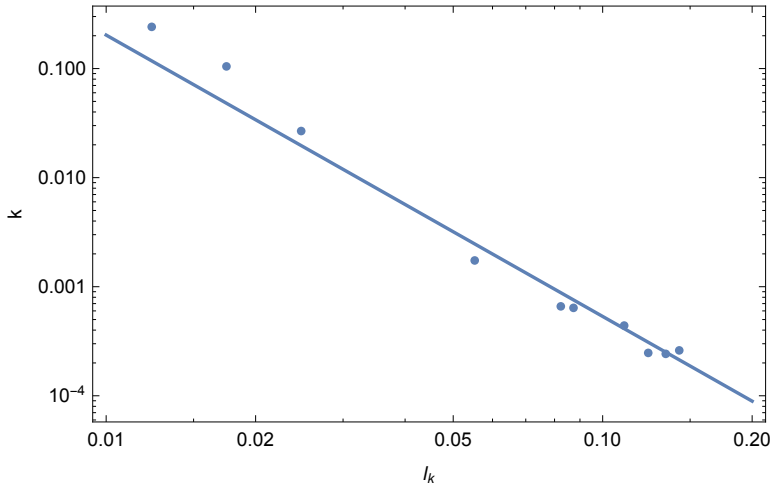

Figure 3.9: Plot of k_1 vs ℓ_k with the fit bx^a where $a = -2.5$ and $b = 1.4 \times 10^{-6}$.

Chapter 4

Distance between Spacetimes

In some theories of quantum gravity spacetime is assumed to have an underlying structure from which spacetimes emerges an approximation. In these theories it is important to show that the spacetime emerging from the underlying structure is approximately isometric to General relativity spacetime in the classical limit. This requires a measure of distance between two spacetimes. In this chapter we will use causal set theory as a tool to measure this distance. In causal set theory the underlying structure of spacetime is a causal set from which spacetime emerges as an approximation.

It is important to have a measure of how much of the structure of a spacetime is captured by a causal set. If a causal set, C, captures most of the structure of the spacetime, then it can not approximate two different spacetimes. This is part of the "main conjecture" (Hauptvermutung) of causal sets which states that: If a causal set C faithfully embeds into two distinct spacetimes, then the two spacetimes are approximately isometric down to the discreteness scale.

A given continuum spacetime (M, g) approximates a causal set C if there is a faithful embedding $\Phi : C \to (M, g)$. An embedding Φ is said to be faithful if it satisfies the following conditions[61, 62]:

i) It is order preserving, that is $\Phi(x) \prec \Phi(y)$ if and only if $x \prec y, \forall x, y \in C$.

ii) The points $\Phi(x)$ are distributed uniformly in (M, g).

iii) The mean spacing between all the embedded points is much smaller than any scale defined by the geometry of (M, g), that is, (M, g) has no structure below the scale ρ^{-1} (ρ is the density of points).

The last two conditions can be interpreted as for $\Phi(C) \subset M$, C has a high probability of being generated by sprinkling on (M, g).

The continuum that is obtained as an approximation does not have geometrical information below the discretization scales (which is usual Plank scale). At distance greater than the discretization scale, a causal set is expected not to approximate two different spacetimes since at this scale the causal set carries all the geometrical information of the spacetime. The formal statement for the Hauptvermutung is then:

Hauptvermutung: *If a causal set C faithfully embeds into two distinct spacetimes (M_1, g_1) and (M_2, g_2) then these spacetimes are related by an approximate isometry.*

When the discretization scale goes to zero ($\rho \to \infty$) a form of the conjecture has been proved by Bombelli *et. al*[63] and for compact spaces [61]. Though the conjecture has not been proved for the general case, a lot of evidence seems to point that this is true even for finite ρ. For example, construction of geometrical and topological information from causal set, obtaining correct dimensional and proper time information[64]. Yazdi and Kempf [94] calculate spectral distance between causal sets and simulations were done for causal sets with $n < 8$.

Even without proving this conjecture, to precisely state it, it is necessary to define closeness of two manifolds, what one means in saying two spacetimes are approximately isometric to each other or approximatetly isometric on scale λ. A lot of work has been done in trying to give a mathematical definition of distance between two spacetimes, a measure of how close two spacetimes are to being isometric[61, 63, 65, 66].

We will follow closely the proposal made by Bombelli [65]. He considers two spacetimes to be close, if the same number of points are random uniformly distributed on both spacetimes, the probability of getting any given induced partial order (causal set) among the points is about the same in both spacetimes.

We will first consider a special case, when the probability of any causal set is exactly the same for the two manifolds. In this case, the manifolds by definition are at distance zero, hence they *must* be isometric. Otherwise one has at best what's called a pseudo-metric. If this fails then something is wrong with our definition of closeness. Hence this special case is a first test of the definition of distance. If it works, the next step is to prove that when the distance is not zero but $\ll 1$, the manifolds are approximately isometric, and when they are approximately isometric the distance is small.

The chapter is structured as follows: In section 4.1 we discuss Bombelli's definition of closeness of two manifolds. A mathematical definition of distance between two manifolds,

using probability distribution that the process of Poisson sprinkling induces on the space of all (finite) causal sets. We then prove then that if two spacetime are isometric then the probability of getting any causal set through the process of Poisson sprinkling is the same for the two manifolds. In section 4.2 considering a finite, globally hyperbolic, compact spacetime, we introduce a process of constructing a sequence of causal sets that are subsets of each other to reconstruct the full continuum spacetime manifold. Obtaining two continuum spacetimes from the same sequence of causal set then implies that two spacetime manifolds are themselves the same. In section 4.3 we then argue that if two manifolds have small distance $\ll 1$, then the two manifolds are approximately isometric. In section 4.3, we do simulations to calculate distance between different spacetimes. In section 4.4, we define faithful embedding and then sketch a proof of the Hauptvermutung.

4.1 Bombelli's distance

The challenge is to find a way to measure how close two spacetimes are to being isometric. We will discuss Bombelli's[65] definition of closeness of two spacetimes. Though its motivation is from causal set theory it can be used for any two spacetimes with any dimensions.

Consider a finite compact spacetime, sprinkle points on the spacetime using Poisson distribution. Keep the causal relation of the points but not their position in spacetime, what you have is a causal set. The causal relations induce an order among the points, this order gives the causal structure of the spacetime and the number of points (causal elements) gives the volume of the spacetimes. In this way, the process of Poisson sprinkling gives a causal set from which the geometry of spacetime can be recovered.

The idea is that, since the sprinkled points (causal set) carry all the metric information upto the discretization scale, then any two spacetimes that are reconstructed from the same causal set will be the same upto the discretization scale. Bombelli defines distance between two manifolds (M, g) and (M', g') using the probability $P_\ell(n, C|(M, g))$ of getting a causal set C, when sprinkling n points on both spacetimes to be

$$d_\ell(M, M') = \frac{2}{\pi} \arccos \left[\sum_{n=0}^{\infty} \sum_{C \in C_n} \sqrt{P_\ell(n, C|(M|g) P_\ell(n, C|(M', g')))} \right]. \tag{4.1}$$

The probability of getting a causal set $C \in C_n$ when sprinkling n elements is given by

$$P_\ell(n, C|(M,g)) = P_\mu(n) P_n(C|(M,g)), \tag{4.2}$$

where C_n is a set of all causal sets with n elements and

$$P_\mu(n) = \frac{e^{-\mu}\mu^n}{n!}, P_n(C|(M,g)) \quad := \frac{n!}{|\mathrm{Aut}(C)|} \frac{1}{V_M^n} \prod_{i=1}^{n} \int_{M_i(x_1,\ldots,x_{i-1};\bar{C})} \sqrt{-g(x_i)} d^D x_i \tag{4.3}$$

where $\mu = V_M/\ell^D$, V_M is the volume of the manifold, $D =$ dimensions of the manifold, $\bar{C}$ is a poset with labelled elements and $M_i(x_1, \ldots, x_{i-1}; \bar{C})$ is the region of integration. For example, if C is a two chain (⁝). The region of integration for the first element would be the whole spacetime and the second would the future light cone of the first element.

$$P_n(⁝|(M,g)) := \frac{2!}{1} \frac{1}{V_M^2} \int_M \sqrt{-g(x_i)} d^D x_1 \int_{I^+_{x_1}} \sqrt{-g(x_i)} d^D x_2 \tag{4.4}$$

The region of integration will depend on the light cones, it changes with change in the metric.

First, we want to consider a special case, when the probability of getting any causal set C from sprinkling n points on the two manifolds (M,g) and (M',g') is the same. In this case we expect that this implies that the two manifolds are isometric, $d_\ell(M,M') = 0$, in scales greater than the descritization scale. It can easily be shown that if the two manifolds (M,g) and (M',g') are isometric then the probability of getting any causal set C in the two manifolds will be the same.

4.1.1 Isometric Spacetime Manifolds

Proposition 4.1.1. If two manifolds (M,g) and (M',g') are isometric then $d_\ell(M,M') = 0$.

Proof. Assume the two manifolds (M,g) and (M',g') are isometric, then $V_m = V'_m$ hence $\mu = \mu' = V_M/\ell^D$. If the sprinklings on both manifolds have the same density. This in turn implies that

$$P_\mu(n) = \frac{e^{-\mu}\mu^n}{n!} = P_{\mu'}(n),$$

for all n. Since the two manifolds are isometric then, there exists a mapping $\Phi : x_i \to x'_i$, that preserves distances and angles. Therefore, $g(x) = g'(x')$

$$\int \sqrt{-g(x_i)}dx_i = \int \sqrt{g'(x'_i)}dx'_i,$$

and light cones do not change hence the regions of integration (M_i's) do not change. The probability of getting causal set C from sprinkling n point on (M, g) is

$$\begin{aligned} p_\ell(n, C|(M,g)) &= P_\mu(n)P_n(C|(M,g)), \qquad (4.5)\\ &= P_\mu(n)\frac{n!}{|\mathrm{Aut}(C)|}\frac{1}{V_m}\prod_{i=1}^{n}\int_{M_i(x_1,\ldots,x_{i-1};\bar{C})}\sqrt{-g(x_i)}d^Dx_i \\ &= P_{\mu'}(n)\frac{n!}{|\mathrm{Aut}(C)|}\frac{1}{V'_m}\prod_{i=1}^{n}\int_{M_i(x'_1,\ldots,x'_{i-1};\bar{C})}\sqrt{-g(x'_i)}d^Dx'_i. \\ &= p_\ell(n, C|(M',g')) \qquad (4.6)\end{aligned}$$

so that

$$\sum_{C\in C_n}\sqrt{P_n(C|(M,g))P_n(C|(M'g'))} = 1, \qquad \sum_n \sqrt{P_\mu(n)P_{\mu'}(n)} = 1.$$

The distance between the two manifolds will then be

$$\begin{aligned} d_\ell(M,M') &= \frac{2}{\pi}\arccos\left[\sum_{n=0}^{\infty}\left(\sqrt{P_\mu(n)P_{\mu'}(n)}\sum_{C\in C_n}\sqrt{P_n(C|M)P_n(C|M')}\right)\right] \\ &= \frac{2}{\pi}\arccos(1) \\ &= 0.\end{aligned}$$

This concludes the prove that if two manifolds are isometric to each other then the probability of getting any causal set C by sprinkling points using Poisson distribution is the same and $d_\ell = 0$. □

Now, we want to show that if the probability distribution of causal sets is the same for two manifolds then the two manifolds are the same. To do this, we will attempt to reconstruct the spacetime from a sequence of causal sets showing if the probability distribution of getting such a sequence of causal sets is the same in both manifolds then the manifolds are the same.

4.1.2 Reconstruction of the continuum from causal sets

To reconstruct a spacetime from a causal sets, ideally one needs a set of causal sets $\mathcal{C}_n$ such that $C_1 \subset C_2 \subset C_3 \subset \ldots C_n$. Reconstruction of spacetime using such causal sets has been done in Reference[61, 63]. However, the probability of getting such a sequence of sprinklings is approximately zero. Now, we will construct a sequence of causal sets that has a high probability of occurring and from which the continuum spacetime can be reconstructed.

Consider a sequence of causal sets obtained by first sprinkling points on M to get a "causal set" C_1'. C_1 is the causal set from C_1' obtained by keeping only causal relations of the points in C_1' and no co-ordinates. Then sprinkle at a higher density to get C_2', such that $\forall x_i \in C_1', \exists y_i \in C_2'$ and $d(x_i, y_i) < d_1$, (where $d(\cdot, \cdot)$ is the Euclidean distance) that is for any $x_i \in C_1'$ there is a $y_i \in B(x_i, d_1)$. To ensure that the open ball $B(y_i, d_2) \subset B(x_i, d_1)$ set $d_1 = d_1' - d_2'$. Consider $d_1 > 0$ but small so that the $B(x_i, d_1)$ do not intersect. Now, sprinkle at even higher density to get C_3', such that for every $y_i \in C_2'$, there exist $z_i \in C_3'$ such that $d(y_i, z_i) < d_2$. Also $d_2 < d_1$, as shown in figure 4.1. Continue such a process at each step increasing the density of points such that we obtain a sequence of causal sets $\{C_1', C_2', \ldots C_n'\}$ with $d_1 < d_2 < \ldots < d_n$. Note that

$$\lim_{i \to \infty} d_i = 0.$$

Proposition 4.1.2. A sequence of sprinklings on a manifold, (M, g) with finite volume, with increasing density at each step can result in a non zero probability of generating a sequence of "causal sets" $\{C_1', C_2', \ldots C_n'\}$ with $d_1 > d_2 > \ldots > d_n$.

Proof. Consider a sequence of poset obtained by first sprinkling points on M using Poisson distribution to get a poset C_1'. Then sprinkle at a higher density to get C_2' and keep repeating the process and increasing density at each step. The mean point spacing is related to the density of points $\rho = \frac{n}{V_M}$ by $\ell^D = \frac{1}{\rho}$. Increasing the density of points decreases the mean spacing between them. The probability that there is no y_j in the open neighbourhood $B(x_j, d_i)$ is give by

$$P_{not} = e^{-\rho V_R} = \exp\left(-\frac{\pi^{D/2} d_i^D}{\Gamma(\frac{D}{2}+1)\ell_{i+1}^D}\right) \tag{4.7}$$

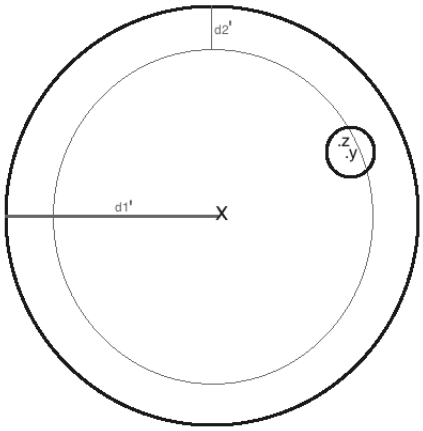

Figure 4.1: Construct a sequence of "causal sets" $\{C'_1, C'_2, \ldots C'_n\}$ in which for every $x_i \in C'_1$ there exist $y_i \in C'_2$ such that $y_i \in B(x_i, d_1)$, and for every $y_i \in C'_1$ there exist $z_i \in C'_2$ such that $z_i \in B(z_i, d_2)$ and $d_1 > d_2 > \ldots > d_n$.

So that the probability of finding y_j inside the ball $B(x_j, d_i)$ is

$$\begin{aligned} P &= (1 - P_{not}) \\ &= 1 - \exp\left(-\frac{\pi^{D/2} d_i^D}{\Gamma(\frac{D}{2}+1)\ell_i^D}\right). \end{aligned} \tag{4.8}$$

Then, the probability of having such a y_j for every x_j is given by

$$\begin{aligned} P &= \prod_{j=1}^{n_i}(1 - P_{not}) \\ &= \prod_{j=1}^{n_i}\left(1 - \exp\left(-\frac{\pi^{D/2} d_i^D}{\Gamma(\frac{D}{2}+1)\ell_{i+1}^D}\right)\right) \\ &= \exp\left(-\exp\left(-\frac{\pi^{D/2} d_i^D}{\Gamma(\frac{D}{2}+1)\ell_{i+1}^D}\right) n_i\right) \\ &= e^{-\Upsilon} \approx 1 - \Upsilon. \end{aligned} \tag{4.9}$$

where $\Upsilon = \exp\left(-\frac{\pi^{D/2} d_i^D}{\Gamma(\frac{D}{2}+1)\ell_{i+1}^D}\right)\frac{V_M}{\ell_i^D}$. In order to have the probability of getting a y_i inside

each ball close to 1, we must choose d_i such that $\Upsilon < \epsilon$, (ϵ being a very small number):

$$-d_i < \ell_{i+1} \left(\ln \left(\frac{\epsilon \ell_i^D}{V_M} \right) \frac{\Gamma\left(\frac{D}{2}+1\right)}{\pi^{D/2}} \right)^{1/D} \tag{4.10}$$

Elements of C_i' will have a mean spacing of $\ell_i > \ell_{i+1}$; hence each element of C_i' will have an element of C_{i+1}' close to it. That is, for every $x_j \in C_i'$, there exists $y_j \in C_{i+1}'$ such that $d(x_j, y_j) < d_i$. Increasing the density of points of C_{i+1}' with a higher factor implies ℓ_{i+1} becomes even smaller. Hence, considering a sequence of sprinklings on manifold (M, g), when the density is increased at each step can result in a non zero probability of obtaining a sequence of causal sets $\{C_1', C_2', \ldots C_n'\}$ with $d_1 < d_2 < \ldots < d_n$. The probability becomes close to 1 if the density is increased by a large factor at each step. □

Each C_i' can be embedded into a C_{i+1}' by shifting each element $x_a \in C_i'$ to $y_a \in C_{i+1}'$ that is inside the ball, $B(x_a, d_i)$.

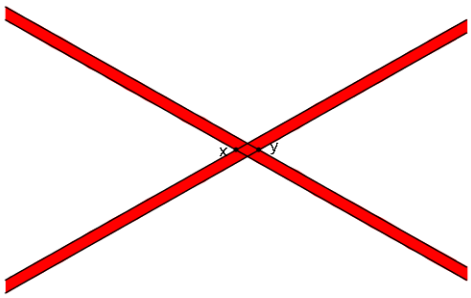

Figure 4.2: When we shift an element of a casual set from x to y, in order not to have elements in the causal future (or past) of x that were original not there, the red region should be empty.

When shifting x to y we require that the elements that were part of the causal future before the shift, remain in the causal future after the shift and those that were not do not become part of the causal future. For this to be true, we would like not to have any x in the red region in figure 4.2. The probability that there is no x in the red region in 2D is given by

$$P = \exp\left(-\frac{4\sqrt{V_M/2}d_i}{\ell_i^2} \right).$$

For this to be very close to 1,

$$d_i \ll \frac{\ell_i^2}{4\sqrt{V_M/2}}. \tag{4.11}$$

For a curved spacetime, varying x_i will also change the light cones. To satisfy the condition that the red region remains small and without any x_j, we want changes in the light cones to be minimal when change in the metric is small, in the order of ϵ.

Proposition 4.1.3. For every ϵ there exist δ such that when the metric field is changed by δ then the light cones do not change by more than ϵ.

Proof. The light cone is characterised by the null geodesic equation

$$\begin{aligned} u^a \nabla_a u^b &= 0, \\ u^a \cdot u^b &= 0. \end{aligned} \tag{4.12}$$

Consider a scalar field f, that is constant everywhere inside the light cone and zero outside, so that on the light cone

$$u_a = \nabla_a f. \tag{4.13}$$

Varying equation (4.12), we have

$$\begin{aligned} \delta\left(u^a \cdot u^b\right) &= 0 \\ \delta g^{ab} u_a u_b + 2 g^{ab} u_a \delta u_b &= 0 \\ \delta g_{ab} u^a u^b &= 2 u^b \delta \nabla_b f \\ \frac{D}{D\lambda}(\delta f) &= \frac{1}{2} \delta g_{ab} u^a u^b \end{aligned} \tag{4.14}$$

Now, relating δf with the light cones

$$\begin{aligned} \delta(f(x)) = (\delta f)(x) + (\delta x \cdot \nabla) f &= 0 \\ \delta x^a \nabla_a f &= -\delta f(x) \\ \delta x^a u_a &= -\delta f(x) \end{aligned} \tag{4.15}$$

So that equation (4.14) now becomes,

$$\begin{aligned} \frac{D}{D\lambda}(-\delta x^a u_a) &= \frac{1}{2} \delta g_{ab} u^a u^b \\ -\left(\frac{D\delta x^a}{D\lambda}\right) u_a &= \frac{1}{2} \delta g_{ab} u^a u^b. \end{aligned} \tag{4.16}$$

This equation tells us where the new light cones are when one varies the metric. Choosing a vector n such that $n \cdot n = 0$, $n \cdot u = -1$ we have

$$\delta x = \nu n,$$
$$u\delta x = -\nu.$$

If the metric is varied, the light cones will change by ν

$$\nu = \int \frac{1}{2}\delta g_{ab} u^a u^b d\lambda. \tag{4.17}$$

This concludes the proof that varying the metric by δ will change the light cones by ϵ. □

Now we have a set of causal sets that can be embedded into each other, C_i into C_{i+1}, through shifts of $x_a \in C_i$ to $y_a \in C_{i+1}$. For causal relations of each causal set not to change it is required that the shift be within the neighbourhood $B(x_a, d_i)$. If the embedding of the causal sets within the neighbourhoods is not the only possible embedding of these causal sets to one another, then how can one distinguish one from the other, because causal sets do not have position information? We would like the embedding within the neighbourhoods to be the only possible embedding or at least have the probability of occurring approximately 1.

One embedding would be having all elements move randomly for distances greater than d_i and remain with the same causal relations and occupy the same volume. In flat spacetime this will not be possible because what ever the random move each point makes can be thought of as a series of translation. Since we require that the points occupy the same volume and the causal relations not to change, then all the elements of the same causal set must have moved the same series of translations. If all the elements of C_i translate to the same direction then those close to edge will leak out, hence this can not be a valid map.

In a curved spacetime even though the series of random moves each causal element makes may not necessarily be a series of translations. Since we require that the points occupy the same volume and the causal relations not to change. This implies that such a map must conserve the the anti-chains. If anti-chains (hypersurfaces) are preserved by such a map, the causal elements can only move within the hypersurfaces. Again if the causal elements near the boundary move away from the boundary, a distance greater than d_i, and greater than the discretization scale, the probability that it gets more elements in its future and its past is close to 1. Unless the elements in the other hypersurfaces also move away from the boundary but this will be decreasing the volume which the causal set occupies.

Another embedding would be if all elements shrink into a smaller region, by the same scale factor. The order relation will be preserved, but there will be in a smaller volume as shown in Figure 4.3. In this case the embedding of C_i into C_{i+1} is not within the neighbourhoods but conserves the causal order for both causal sets. We would like the probability of such an embedding to be small. First let us calculate how likely it is that if one chooses an embedding of C_i on C_{i+1} at random the embeddingis is the neighbourhood embedding. The expectation value of number of $y_i's \in C_{j+1}$ in the neighbourhood $B(x_i, d_j)$ will be given by

$$\begin{aligned}\mathcal{C}_A &= \nu_i \\ &= \pi \left(\frac{d_i}{l_{i+1}}\right)^2\end{aligned}$$

$d_i > \ell_{i+1}$,so that the expectation value number of copies of C_i inside the $B(x_i, d_j)$ will be

$$\begin{aligned}\langle \mathcal{C}_A \rangle &= \prod_{i=1}^{n_i} \langle \nu_i \rangle \\ &= \pi^{n_i} \left(\frac{d_i}{l_{i+1}}\right)^{2n_i}.\end{aligned} \tag{4.18}$$

Consider a copy of C_i in some region B, with volume $V_B = \frac{V_A}{R}$, where V_A is the volume of the manifold. The expectation value for number of such regions B with copies of C_i is,

$$\langle \mathcal{C}_B \rangle = \pi^{n_i} \left(\frac{d_i}{l_{i+1}}\right)^{2n_i} \frac{1}{R^{2n_i}}. \tag{4.19}$$

The expectation value of finding a copy of C_i in C_{i+1} in the small region B is smaller than that of finding it in A by a factor of $\frac{1}{R^{2n_1}}$. Therefore, in general we expect the embedding within the neighbourhoods $B(x_i, d_j)$ to be highly likely than any other embedding.

Now that we have sketched how to construct the desired set of causal sets, let us restate and argue further for the conjecture.

Conjecture 4.1.1. If the distace between two manifolds, (M, g) and (M', g'), is zero then the two manifolds are isometric.

Evidence.
Consider a sequence of causal sets generated by sprinkling points on a globally hyperbolic

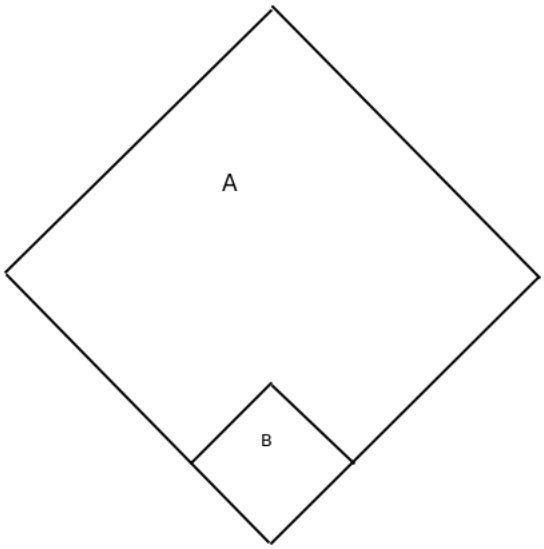

Figure 4.3: C_i might embedded into a C_{i+1} in a smaller region, B.

manifold, M, as discussed in Figure 4.1. Then each C_i can be embedded into C_{i+1}, so that in taking the direct limit

$$\cup_{i=1}^{\infty} C_i = C_\omega. \tag{4.20}$$

Note that C_ω is dense in (M, g). Since M is a compact space then all sequences in C_ω have a sub-sequence that converge. Adding all limit point (avoiding duplication) of sequences in C_ω that are not in C_ω, in analogy with the Dedekind cut construction of real numbers, we obtain all the points of the manifold with their causal relations, recovering the continuum spacetime. The equality of all $P_n(C|M) = P_n(C|M')$ implies the causal sets probability of getting each C_i in C_ω a union of causal sets generated by sprinkling M and will be same as the probability of getting each C_i in C'_ω a union of causal sets generated by sprinkling M'. A completion based on C_ω will give the same points and causal relation for the two manifolds, implying that (M, g) is isometric to (M', g'). □

4.2 Approximately Isometric Spacetimes

If the Bombelli distance is a good measure then if two spacetimes are approximately isometric then the distance between the two of them is small ($\ll 1$), that is, the probabilities

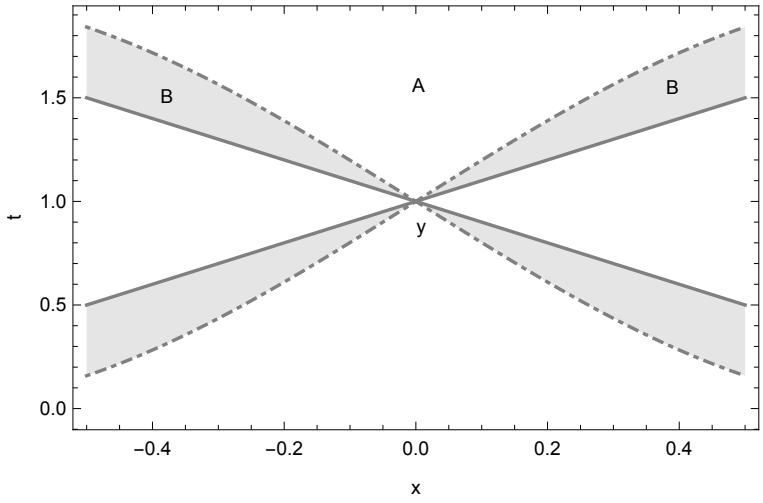

Figure 4.4: Split the region of integration in M' to be the region of integration in M plus the region the coloured region between the two null lines. The volume of the causal future of y in M' is $A = I^+(y|M) - B$.

do not differ by much. To show this we consider sprinklings on the two spacetimes on a region $\mathcal{M}$, that has the same volume in both manifolds, M and M'. So that $P_\mu(n) = P_{\mu'}(n)$. Also consider $g' = g + \delta g$ then

$$\begin{aligned} p_n(C|(M',g')) &= \frac{n!}{|\mathrm{Aut}(C)|}\frac{1}{V_m^n}\prod_{i=1}^{n}\int_{M_i'(x_1',\ldots,x_{i-1}';\bar{C})}\sqrt{-g'(x_i')}d^Dx_i' \\ &\approx \frac{n!}{|\mathrm{Aut}(C)|}\frac{1}{V_m^n}\prod_{i=1}^{n}\int_{M_i'(x_1',\ldots,x_{i-1}';\bar{C})}\left(\sqrt{-g(x_i)}+\frac{1}{2}\sqrt{-g(x_i)}\delta g_{ab}g^{ab}\right)d^Dx_i \end{aligned} \tag{4.21}$$

The region of integration $M_i'(x_1', \ldots, x_{i-1}'; \bar{C})$ depends on the labelled causal set $\bar{C}$. The first element x_1 may fall anywhere in the manifold so that for this point $M_1' = M_1$ since (M, g) and (M', g') have the same volume. If the next element, x_2, is causally related to x_1, it must fall in the future of x_1. For x_2 the region $M_2' = I_1^+$. If x_1 and x_2 are not causally related then $M_2' = M \setminus I_1^+$. The limits of integration, $(\int_{\text{limit}} dx_j)$ are the points where the null geodesics passing through x_j cross the boundary of the manifold.

Assuming that the manifold is compact globally hyperbolic, the region of integration (M', g') can be split into two as shown in Figure 4.4: integrate with limits that are the same as the limits in for the integrals in (M, g) and the volume between the two geodesics will be the integral of the change in the null geodesics given by equation(4.17).

$$p_n(C|(M',g')) = \frac{n!}{|\mathrm{Aut}(C)|}\frac{1}{V_m^n}\prod_{i=1}^{n}\left[\int_{M_i(x_1,\ldots,x_{i-1};\bar{C})}\left(\sqrt{-g(x_i)}+\frac{1}{2}\sqrt{-g(x_i)}\delta g_{ab}g^{ab}\right)d^Dx_i \right.$$
$$\left. + \int \frac{1}{2}\delta g_{ab}u^a u^b d\lambda\, d^{D-1}x_i\right] \tag{4.22}$$

When $\delta g = 0$, that is, $g' = g$ then $P_n(C|(M,g)) = P_n(C|(M',g'))$, hence the distance between the two manifolds is zero. If $\delta g \neq 0$ but very small, so that we can neglect term with $(\delta g)^2$ then;

$$\begin{aligned}
P_n(C|(M',g')) &= \frac{n!}{|\mathrm{Aut}(C)|}\frac{1}{V_m^n}\prod_{i=1}^{n}\int_{M_i(x_1,\ldots,x_{i-1};\bar{C})}\sqrt{-g(x_i)}\,d^Dx_i \\
&+ \frac{n!}{|\mathrm{Aut}(C)|}\frac{1}{V_m^n}\sum_{j=1}^{n}\left[\prod_{i=1}^{j}\int_{M_i(x_1,\ldots,x_{i-1};\bar{C})}\sqrt{-g(x_i)}\right. \\
&\times \left.\left(\int_{M_j(x_1,\ldots,x_{i-1};\bar{C})}\frac{1}{2}\sqrt{-g(x_j)}\delta g_{ab}g^{ab}\left(\prod_{k=j+1}^{n}\int_{M_k(x_1,\ldots,x_{i-1};\bar{C})}\sqrt{-g(x_i)}d^Dx_i\right)d^Dx_j\right)d^Dx_k\right] \\
&+ \frac{n!}{|\mathrm{Aut}(C)|}\frac{1}{V_m^n}\sum_{j=1}^{n}\left[\prod_{i=1}^{j}\int_{M_i(x_1,\ldots,x_{i-1};\bar{C})}\sqrt{-g(x_i)}\right. \\
&\times \left.\left(\int_{M_j(x_1,\ldots,x_{i-1};\bar{C})}\frac{1}{2}\sqrt{-g(x_j)}\delta g_{ab}u^au^bd\lambda\left(\prod_{k=j+1}^{n}\int_{M_k(x_1,\ldots,x_{i-1};\bar{C})}\sqrt{-g(x_i)}d^Dx_i\right)d^{D-1}x_j\right)d^Dx_k\right] \\
&+ \mathcal{O}(\delta g^2) \\
&= P_n(C|(M,g)) + \mathfrak{E}(\delta g) + \mathcal{O}(\delta g^2).
\end{aligned} \tag{4.23}$$

If the two metrics differ by δg, then the leading term in the difference of the P_ns will be of order δg. We expect that if δg is small the distance between the two manifolds will also be small.

$$\begin{aligned}
d_\ell &= \frac{2}{\pi}\arccos\left[\sum_{n=0}^{\infty}\left(\sqrt{p_\mu(n)p_\mu(n)}\sum_{C\in C_n}\sqrt{P_n(C|M)^2 + P_n(C|M)\mathfrak{E}(\delta g)}\right)\right] \\
&= \frac{2}{\pi}\arccos\left[\sum_{n=0}^{\infty}\left(\sqrt{p_\mu(n)p_\mu(n)}\sum_{C\in C_n}\left(P_n(C|M) + \frac{1}{2}\mathfrak{E}'(0)\delta g + \mathcal{O}(\delta g^2)\right)\right)\right] \\
&= 0 + \frac{2}{\pi}\arccos\left[\sum_{n=0}^{\infty}\left(\sqrt{p_\mu(n)p_\mu(n)}\sum_{C\in C_n}\left(P_n(C|M)\frac{1}{2}\mathfrak{E}'(0)\delta g + \mathcal{O}(\delta g^2)\right)\right)\right] \\
&\approx 0.
\end{aligned} \tag{4.24}$$

4.3 Simulations: Distance between spacetimes

In this section we use simulations to calculate distance between spacetimes. We did simulation to get the probability distribution for causal sets with two elements, C_2 in a 2D cylinder with diameter a and height b and in a square $[0, a] \times [0, b]$. Even with only two causal element the difference between these two spacetimes starts to show up if the time interval is comparable to the space interval. Figure 4.5a shows that for values of very large or very small $\gamma = b/a$ the probability of getting a chain is approximately the same as the probability of getting an anti-chain in both the cylinder and a square. Figure 4.5b shows that the distance (Bombelli distance in equation 4.1) between the two spacetimes is larger when $\gamma \approx 1$. Having more causal elements gives more information about the spacetimes. For the same spacetimes the distance becomes larger when $n = 3$ than when $n = 2$.

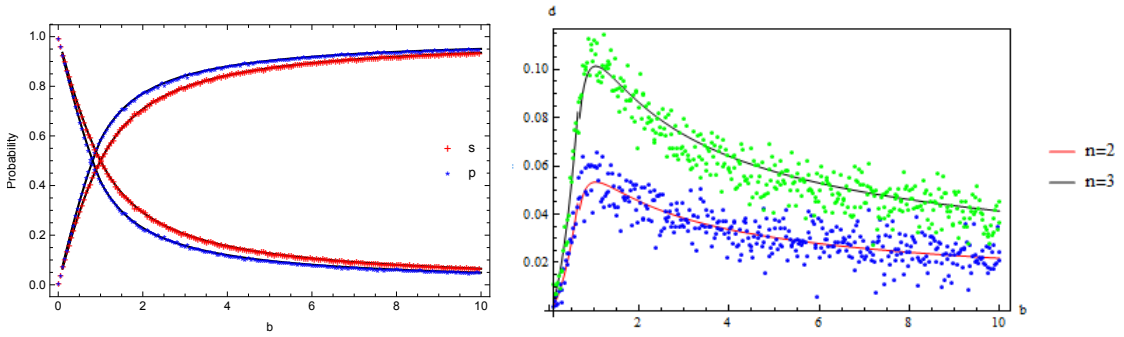

(a) Probability distribution for C_2.

(b) Distance between cylinder and a square.

Figure 4.5: (a) Shows the probability of getting a chain (anti-chain) when two points are sprinkled on a clylinder and a square for $a = 1$. As γ becomes large the probability of getting a chain becomes large and of getting an anti-chain small. The solid lines are analytical values of the probability. (b) Shows distance between the cylinder and a square for different time intervals for $a = 1$.

Figure 4.6a shows distance between: square, diamond, left-triagle of the diamond, upper triangle of the diamond and a cylinder. It shows that as the number of elements increases the distance increases, because having more causal elements implies having more information about the sapcetime. It is computational expensive though to calculate the probability distribution for such large n since the number of causal sets will be very large. For example for $n = 9$ there are 183 231 casual sets, hence one would be required to do about $1.83\,231 \times 10^{12}$ sprinklings inorder to get the probability distributions.

These examples have few number of causal element, n, random uniform distribution has no meaning in this case. If $n \gg 1$, we resort to not using all the information in the causal set. For example, binning the causal sets using the number of relations in a causal set. This does not use most of the information from the causal sets and can not distinguish manifolds with the same number of relations. As shown in Figure 4.7b increasing the number of elements gives more information about the manifold. The probability distributions for the number of relations separate as the number of elements increases except for a square and diamond since they have the same number of causal relations.

Figure 4.6b shows the distance between manifolds using number of relations binning. When $n = 150$, the distance between different manifolds is approximately 1, except for a square and diamond. This is because for a square and diamond the probability that two causal elements are related is the same. Hence as shown in figure 4.7b the histograms for a square and diamond have the same mean. The information that is different between the two is the standard deviation.

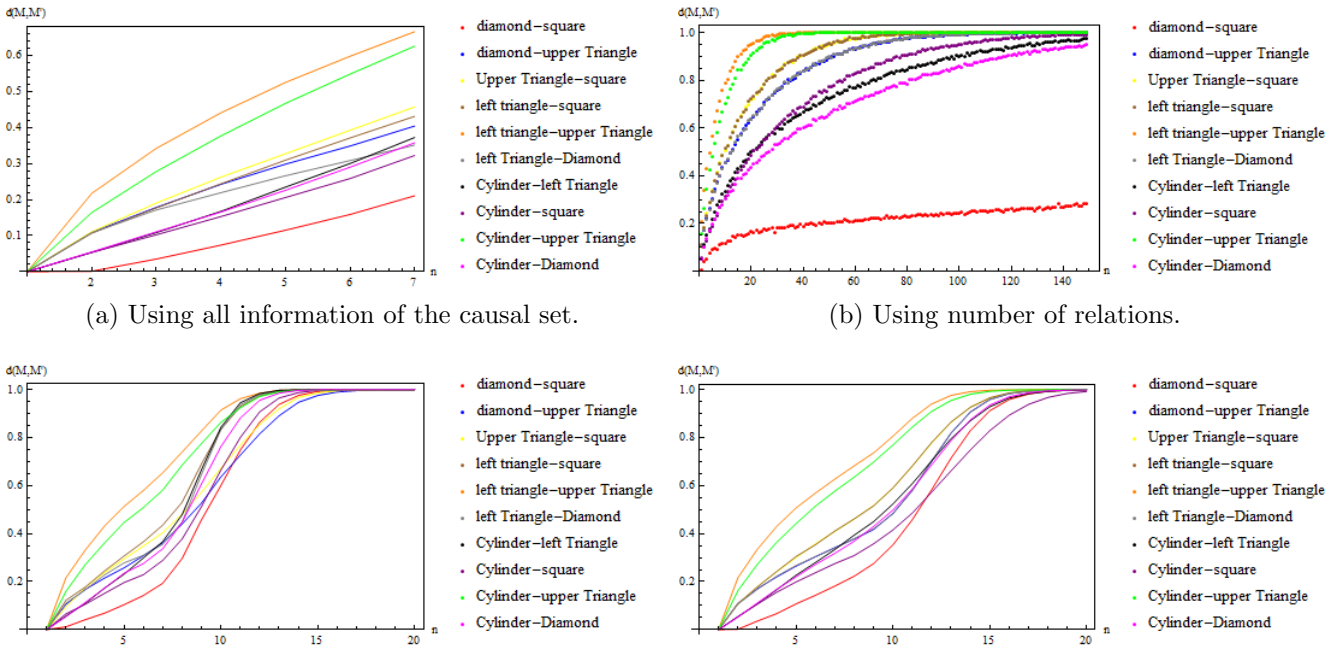

(a) Using all information of the causal set.

(b) Using number of relations.

(c) Using volume of causal interval.

(d) Using volume of past and future.

Figure 4.6: Distance between spacetimes.

Figure 4.6c shows distance obtained when binning using volume of interval. For a pair of elements $x, y \in C$, the volume interval $I(x, y) = \text{Fut}(x) \cap \text{Past}(y)$ is the number

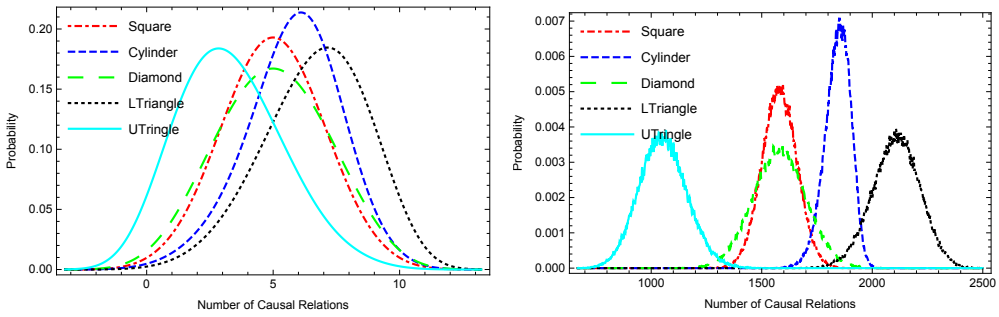

(a) n=5. (b) n=80.

Figure 4.7: Histogram: as n increases, probabilty distributions for manifolds with different number of causal relations separate.

of elements that are in the past of x and in the future of y. In this case the square is different from a diamond. For $n > 7$ the number of bins becomes too large and it becomes computational expensive to get the probability distributions. In Figure 4.6c the distance for $n > 7$ can not be trusted for this reason.

The number of causal elements (n) corresponds to volume when the causal elements are uniformly distributed in spacetime. If n is a very small number then random uniform distribution has no meaning and the number of causal elements does not correspond to the volume of the spacetime.

Characteristics of the Bombelli distance given in equation 4.1 (we will now denote as d_B),

i) d_B is normalized $0 \leqq d_B(M, M') \leqq 1$

ii) $d_B(M, M') = 0$ implies that the two manifolds M and M' are the same up to the desensitization scale.

iii) $d_B(M, M') = 1$ implies that the two manifolds M and M' are are different.

Characteristics of the Relative Entropy distance, $d_{Entropy} = \sum_i p_i \log(p_i/q_i)$,

i) d_E is not normalized.

ii) $d_E(M, M') = 0$ implies that the two manifolds M and M' are the same up to the desensitization scale.

n	2	3	4	5	6
N	2	5	16	63	318
d_B	$0.055 \pm 2 \times 10^{-5}$	$0.105 \pm 5 \times 10^{-5}$	$0.155 \pm 1.6 \times 10^{-4}$	$0.204 \pm 6.3 \times 10^{-4}$	$0.256 \pm 3.1 \times 10^{-3}$
$d_{Entropy}$	$0.015 \pm 2 \times 10^{-5}$	$0.054 \pm 5 \times 10^{-5}$	$0.116 \pm 1.6 \times 10^{-4}$	$0.197 \pm 6.3 \times 10^{-4}$	∞

Table 4.1: Table for distances between a square and a cylinder in 1+1D. n is the number of causal elements and N is the number of causal sets with n elements.

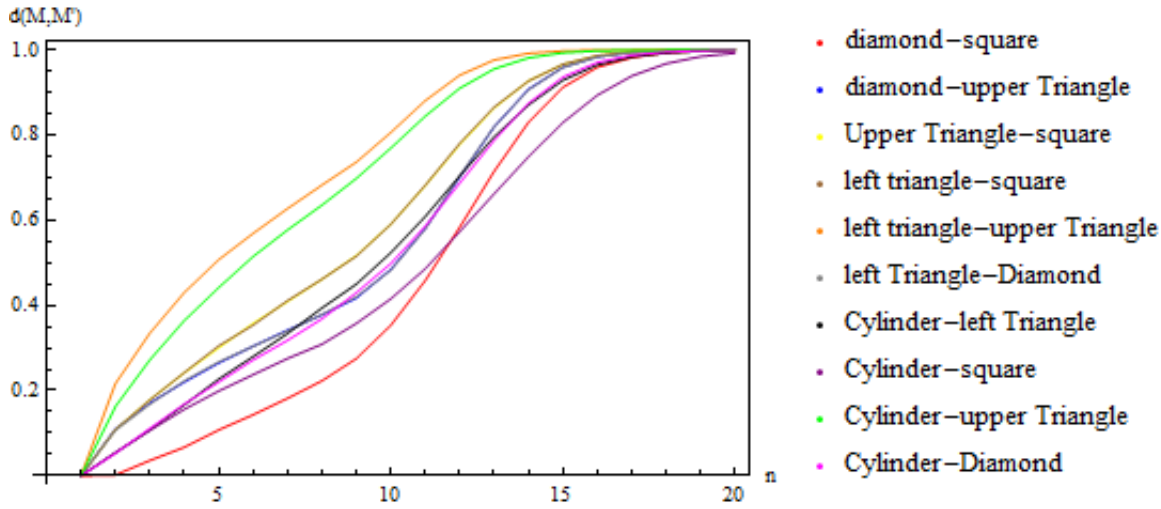

Figure 4.8: Bombelli Distance between different manifolds vs the number of causal elements n using PF Invariant.

ii) $d_E(M, M') = \infty$ implies that the two manifolds M and M' are very different.

The entropy distance between a square and cylinder goes to infinity for $n > 6$ because a cylinder embeds some causal sets that a square does not (Betti number > 1).

The binning we have used so far seem to be computational expensive as number of causal elements is increased. We need binning that comes with a new distance that can be computed for large causal sets. We bin causal sets that have the same past-future sets (PF Invariance). A causal set with n elements is represented as

$$C_n : ((p_1, f_1), (p_2, f_2), (p_3, f_3) \cdots (p_n, f_n)) \tag{4.25}$$

where p_i is the number of causal elements in the past of the i^{th} element and f_i is the number of causal elements in the future of the i^{th} element.

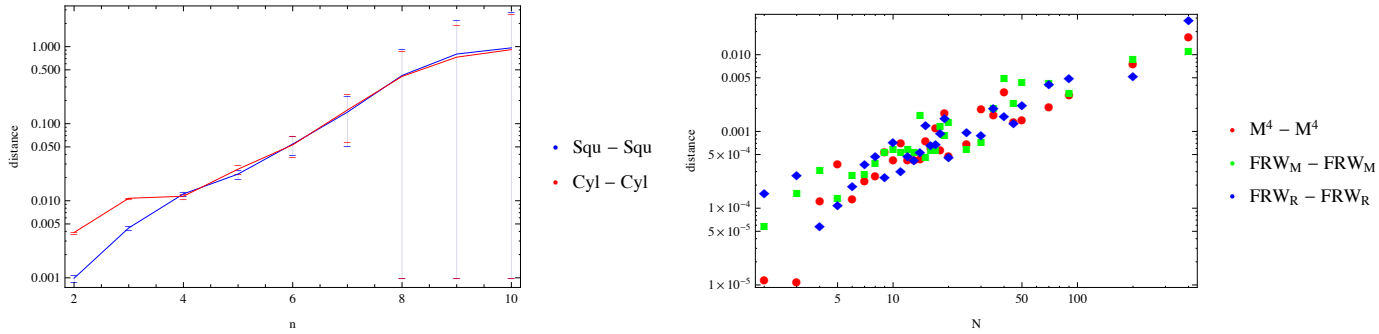

(a) Bombelli Distance

(b) Hellinger Distance

Figure 4.9: Distance between same manifolds. As shown in 4.9a for Bombelli distance the standard deviation is close to 1 for $n > 7$ so these results can not be trusted.

4.3.1 PF Invariant

A new distance, the Bhattacharyya distance is used since Bombelli distance is computational expensive for large causal sets. Instead of mapping to a circle like in Bombelli distance, we calculate the distance between causal sets in the (p, f) space, which will have $2n$ dimensions.

$$d_{pf} = \left(\sum_i \left[(p_i - p_i')^2 + (f_i - f_i')^2 \right] \right)^{1/2} \tag{4.26}$$

Sprinkling a number of times on the same manifold will give a distribution for each point (p_i, f_i), giving a multidimensional distribution. Using Battacharyya distance for Gaussian distributions p and q, the distance between them is

$$D_B(p, q) = -\ln(BC(p, q)), \qquad BC(p, q) = \sum \sqrt{p(x)q(x)}\, dx \tag{4.27}$$

The Bhattacharyya coefficient $0 \leqq BC \leqq 1$ and the distance $0 \leqq D_B \leqq \infty$ does not obey triangular inequality, but the Hellinger distance $\sqrt{1 - BC}$ does. For normal distributions

$$d_H = 1 - \sqrt{\frac{2\sigma_p \sigma_q}{\sigma_p^2 + \sigma_q^2}} \exp\left(-\frac{1}{4} \frac{(\mu_p - \mu_q)^2}{\sigma_p^2 + \sigma_q^2} \right) \tag{4.28}$$

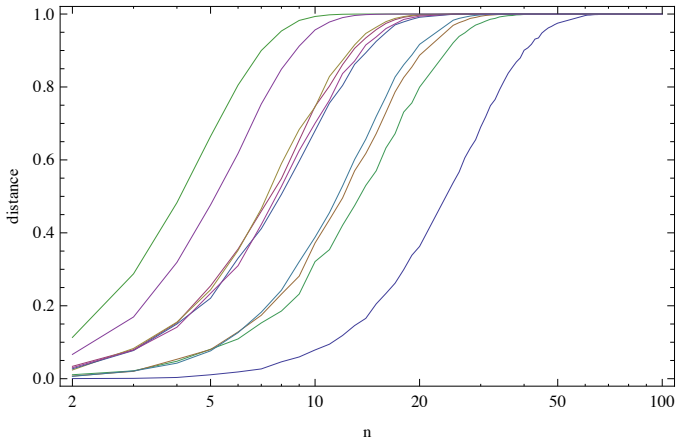

Figure 4.10: Hellinger Distance between different manifolds vs the number of causal elements n using PF Invariant.

where μ is the mean of the distribution and σ^2 is the variance. For multidimensional distributions

$$d_H = 1 - \left(\frac{\sqrt{\det \Sigma_p \det \Sigma_q}}{\det \Sigma_p} \right)^{1/2} \exp\left(-\frac{1}{8} (\mu_p - \mu_q)^T \Sigma \, (\mu_p - \mu_q) \right) \tag{4.29}$$

where Σ_p is the covariance matrix for distribution p and $\Sigma = \frac{\Sigma_p + \Sigma_q}{2}$. The Hellinger measure distinguishes all 5 manifolds as shown in Figure 4.10 when computed in 2^n (p, f) space. Figure 4.9b shows that the distance between a square with volume=1 and a square with volume=1, is close to zero for $n = 50, d_\ell = 0.02$, therefore the results exhibited in Figure 4.10 can be trusted.

Figure 4.11 shows distance between a square and 4D box with the same volume. Figure 4.12 shows the distance between the following 4D manifolds:

$$ds^2 = -dt^2 + dx^2 + dy^2 + dz^2, \quad \text{(Flat spacetime, } M^4\text{)} \tag{4.30}$$

$$ds^2 = -dt^2 + t^{4/3} \left(dx^2 + dy^2 + dz^2 \right), \quad \text{(matter dominated, FRW}_M\text{)} \tag{4.31}$$

$$ds^2 = -dt^2 + t \left(dx^2 + dy^2 + dz^2 \right), \quad \text{(radiation dominated, FRW}_R\text{)} \tag{4.32}$$

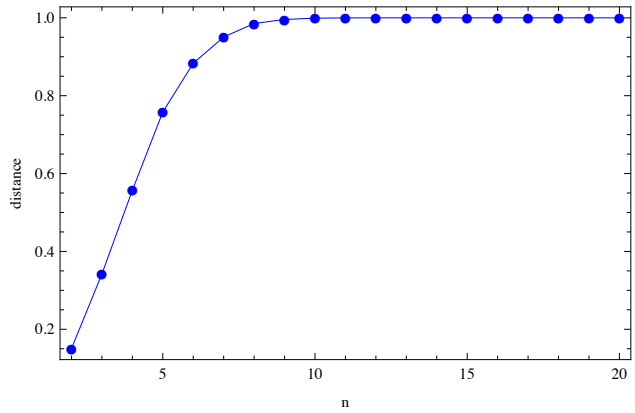

Figure 4.11: Hellinger Distance between different $\mathbf{M}^2$ square and $\mathbf{M}^4$ box with the same volume.

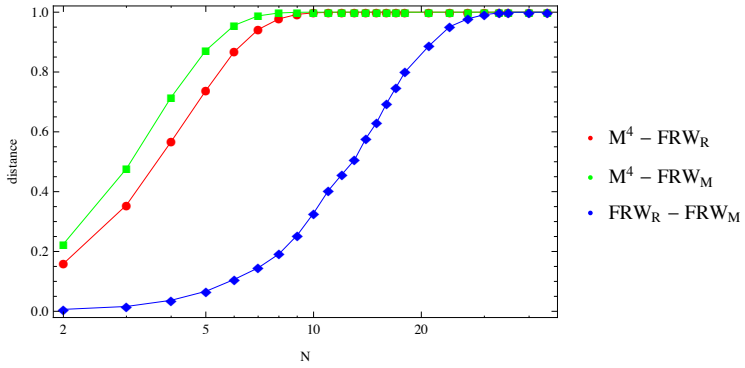

Figure 4.12: Hellinger Distance between different manifolds vs the number of causal elements N using PF Invariant.

4.4 Faithful Embedding

In the examples in section 4.3 we see that different spacetimes have different causal sets with high probabilities. Let us denote the family of causal sets with high probability of being generated when one sprinkles on the spacetime to be, C_h. A causal set encodes the geometry and topology of spacetime. Therefore, causal sets in the the family, C_h, are expected to have some similarities in their causal order since most of the geometry information is encoded in the causal order. Their topological structure, that is sets of anti-chains should also have some similarities. For a cylinder C_h contains casual sets with edges crossing not in vertexes while for a square C'_h contains few of these, with minimal crossings. This is mainly because the cylinder "has back and front sheets" while a square does not have this property it is only one "sheet". For $n \geq 6$, there are causal sets that can be embedded into a cylinder but not a square, these are causal sets with non-zero betti number (b_1), this is discussed in more details in [67]. Using C_h, we a define faithful embedding to be:

Definition 4.4.1. A causal set C faithfully embeds into a spacetime (M, g), if $C \in C_h$, where C_h is a family of causal sets that one is most likely to get (have high probability) from a process of Poisson sprinkling on (M, g).

When number corresponds to volume: we expect that if (M, g) and (M', g') are different then $C_h \cap C'_h = \emptyset$ and if (M, g) is isometric to (M', g') then $C_h \subseteq C'_h$.For small n we do not expect to see $C_h \cap C'_h = \emptyset$ if the two spacetimes are different. The sum of the probabilities in C_h are expected to be large. We take $P(C_h) \geq 0.8$. There is no special reason for choosing this number, we only know that $P(C_h)$ must be large.

Consider a cylinder and a square with same volume. As shown in figure 4.7b, as n increases $C_h \cap C'_h$ becomes a small for different manifolds.

With this definition of faithful embedding and closeness of spacetime the Hauptvermutung conjecture then becomes true by definition.

Hauptvermutung: *If a causal set C faithfully embeds at the same density into two distinct spacetimes (M, g) and (M', g') then these spacetimes are related by an approximate isometry.*

Proof. Consider a causal set C that faithfully embeds to two spacetimes (M, g) and (M', g'). By definition of faithful embedding, $C \in C_h$ in (M, g) and $C \in C'_h$ in (M', g'). This implies that $C'_h \cap C_h \neq \varnothing$, as proposed above then either $C_h \subseteq C'_h$ or $C'_h \subseteq C_h$. Without loss of generality, consider $C_h \subseteq C'_h$, we have $P_\ell(n, C|M, g) \sim P_\ell(n, C|M', g')$ for any $C \in C_h$.

Also, $P(C_h)$ is large, about 80% of the probabilities, so that even if the remaining $C's \notin C_h$ have different probabilities, there difference will be small since they are small as well. For $C \notin C_h$ $P_\ell(n, C|M, g)$ $P_\ell(n, C|M', g') = 0$ (worse case) .

$$\begin{aligned} d_\ell(M, M') &= \frac{2}{\pi} \arccos \left[\sum_{C \in C_n} \sqrt{P_\ell(n, C|(M, g)) P_\ell(n, C|(M, g))} \right] \\ &\approx \frac{2}{\pi} \arccos \left[0.8 + \sum_{C \notin C_h} \sqrt{P_\ell(n, C|(M, g)) P_\ell(n, C|(M, g))} \right] \\ &\approx 0. \end{aligned} \tag{4.33}$$

The two spacetimes are approximately isometric at scales greater than ρ^{-1}. □

We have looked at Bombelli's definition of distance between two spacetimes and proved that with this definition if two spacetimes are isometric then the distance between them is zero. We also showed that if the metrics of two spacetimes differ by very small amount then the two spacetimes will be approximately isometric. We used probability of getting a causal set when sprinkling points on spacetime to define faithful embedding and then used this definition to sketch a proof of Hauptvermutung.

Faithful embedding is not well defined, since it contains, the family C_h which is not well understood. Further work would be to study carefully the properties of C_h. Understanding this family of causal sets would help classify causal sets that are expected to be manifold like, that is have a continuum approximation at microscopic scales. Further more, an understanding of this family might shed light to on how to sum over all causal sets in quantum gravity.

Chapter 5

AdS/CFT Correspondence in relation to causal sets

In AdS/CFt correspondence one considers a Conformal Field Theory (CFT) on the boundary of Anti-de Sitter (AdS) space which corresponds to the gravitational theory on the bulk[68]. In causal set theory one assumes that the causal structure carries all the information about the spacetime[1] . For two spacetime manifolds to have corresponding theories would imply that their causal structures have similarities. The proposal in this case would imply that the causal structure of AdS and its boundary have similarities.

Conjecture: In the limit of infinite coarse graining, AdS has the same causal structure as its boundary.

Let us consider in AdS_3 two events $p_1(\tau_1, \theta_1, \phi_1) \prec p_2(\tau_2, \theta_2, \phi_2)$ in global co-ordinates, with the line element

$$ds^2 = R^2 \sec^2\theta \left(-d\tau^2 + d\theta^2 + \sin^2\theta d\phi^2\right). \tag{5.1}$$

These events are causally related if there is a causal curve joining them, that is,

$$\tau_2 - \tau_1 \geqslant \sin\theta_1 \sin\theta_2 \cos(\phi_2 - \phi_1) + \cos\theta_1 \cos\theta_2. \tag{5.2}$$

If these events are both projected to the boundary, $\theta \to \pi/2$, then they will be causally related $p_1'(\tau_1, \phi_1) \prec p_2'(\tau_2, \phi_2)$ if

$$\tau_2 - \tau_1 \geqslant (\phi_2 - \phi_1). \tag{5.3}$$

[1] excluding conformal volume information

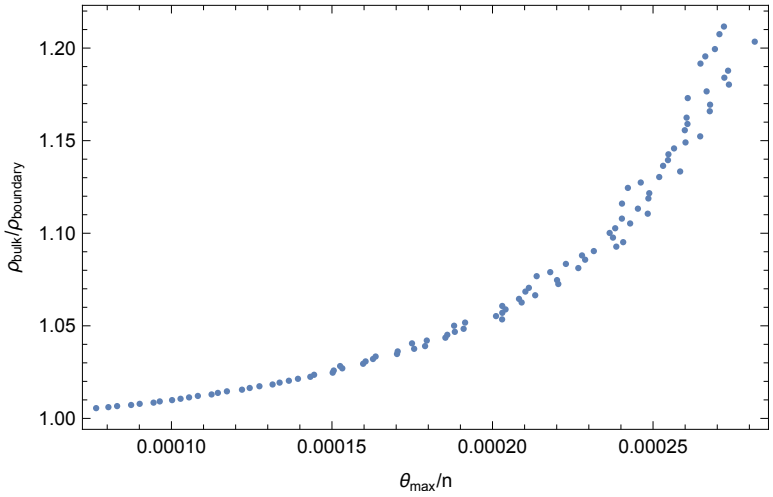

Figure 5.1: Most causal elements are generated by sprinkling points near the boundary. ρ_{bulk} is the density of points on the bulk and $\rho_{boundary}$ is the density of point sprinkled on the thickened boundary. Increasing θ_{max}/n incearses the thicked boundary.

The probability that if $p_1 \prec p_2$ then $p_1' \prec p_2'$ is not equal to one. That is some points that were causally related in the bulk will not remain causally related after the projection. Generating a causal set by sprinkling to AdS, since most of the volume is in the boundary, most sprinkled points will be near the boundary. Figure 5.1 shows that most sprinkled points will be near the boundary, therefore majority of pairs of causal elements that were causally related after the projection will remain causally related. It also shows that as density decrease most points will be near the boundary. For a fixed number of causal elements if the volume increases the sprinkling decreases. Figure 5.2 shows that in the limit as the sprinkling density decrease, that is θ_{max} or the volume increases the probability that two causal elements that were causally related remain causally related is asymptotes to 1.

Considering the Poincare patch of AdS, these co-ordinates do not cover the whole of AdS as shown in Figure 5.3.

$$ds^2 = \frac{R^2}{z^2}\left(-dt^2 + dx^2 + dz^2\right). \tag{5.4}$$

Two events in the bulk will be considered causally related $p_1(t_1, x_1, z_1) \prec p_2(t_2, x_2, z_2)$, if

$$t_2 - t_1 \geqslant \sqrt{(x_2 - x_1)^2 + (z_2 - z_1)^2}. \tag{5.5}$$

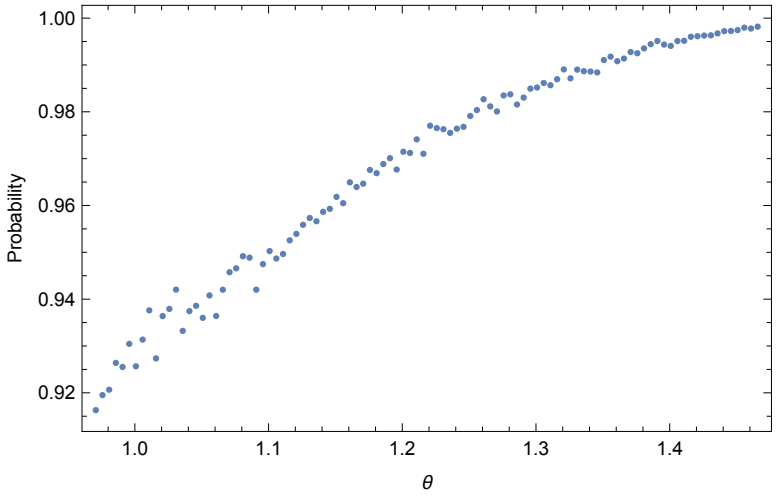

Figure 5.2: Number of pairs related before and after projection divided by number of pairs related before projection.

If these events are both projected to the boundary, $z \to 0$, then they will be causally related $p_1'(t_1, x_1) \prec p_2'(t_2, x_2)$ if

$$t_2 - t_1 \geqslant (x_2 - x_1). \tag{5.6}$$

The probability that if $p_1 \prec p_2$ then $p_1' \prec p_2'$ is equal to 1 in the Poincare patch. The AdS/CFT correspondence usually assumes that the region $z = 0$ plus some isolated points at infinity is the boundary of the Poincare patch. Since the isolated points do not carry degrees of freedom, the correspondence between a field theory in the Poincare patch and a theory on $z = 0$ is taken as a bulk/boundary correspondence.

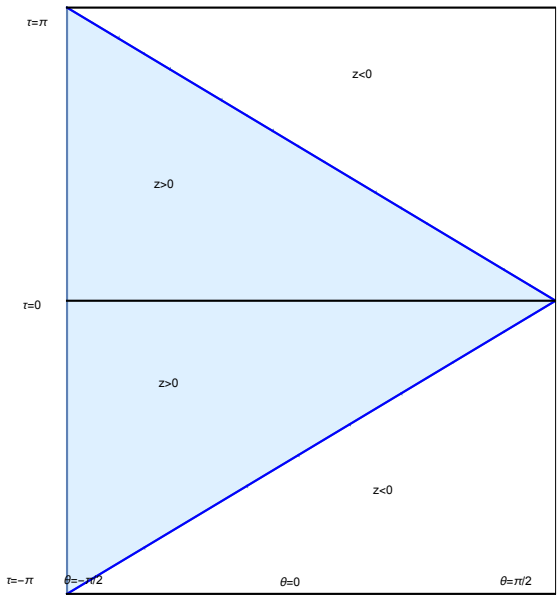

Figure 5.3: Penrose diagram for AdS space, the Poincare AdS is the lightblue region with a boundary at $z = 0$.

Chapter 6

Conclusion

We have discussed different Cosmological test of causal set theory phenomenology, postulating that the fundamental structure of a spacetime manifold is a Lorentz invariant discrete structure endowed with a causal order. Everpresent Λ, model of dark energy, a consequence of Lorentz invariant discreteness predicts that cosmological constant is everpresent and fluctuates with time. Any model of Everpresent Λ is by definition inherently stochastic. As such, it will have many realizations that are different from our own cosmos. Simulations show that there are also many realizations that broadly resemble reality, including some that agree as well as ΛCDM does with several pieces of observational evidence, including CMB measurements. It also eases certain tensions that arise with BAO measurements, measurements of nuclear abundances, and the very early occurrence of ultramassive black holes. If Λ really is fluctuating and "everpresent", that should become more clearly evident as observations accumulate for high redshift.

A signature of Lorentz invariant discreteness implies that the causal set elements are randomly distributed, so that a massive particle propagating on causal set will undergo diffusion in momentum space inducing secondary diffusion in the position space. The diffusion process will have only one parameter, the diffusion constant, k, for which the highest bound comes from the cosmic neutrinos, $k \lesssim 10^{-61}$ and is related to the nonlocality scale τ_f by $k \sim \frac{m^2 d_{pl}^4}{\tau_f^5}$ both in 2D and 3D.

Modeling a particle as wave packet and using causal set discrete D'Alembert operator $\Box\phi(x) \sim B_\epsilon\phi(x)$ to propagate the wave packet has proved to be difficult because of the cut-off introduced by using a finite causal set. Simulations suggest that there is no drift $k_2 \sim 0$ and $k_1 \propto \ell_k^{-2.5}$ in 2D.

We also looked at Bombelli's definition of distance between two spacetimes and showed that with this definition if two spacetimes are isometric then the distance between them is zero. We also argued that if the metrics of two spacetimes differ by very small amount then the two spacetimes will be approximately isometric. We used probability of getting a causal set when sprinkling points on spacetime to define faithful embedding and then used this definition to sketch a proof of Hauptvermutung.

In AdS/CFT correspondence one considers a Conformal Field Theory (CFT) on the boundary of Anti-de Sitter (AdS) space which corresponds to the gravitational theory on the bulk[68]. Two spacetime manifolds having corresponding theories implies that their causal structures have similarities. Simulations suggest that, in the limit of infinite coarse graining, AdS_3(Poincare patch) has the same causal structure as its boundary.

References

[1] . Aubourg et al., *Cosmological implications of baryon acoustic oscillation measurements*, *Phys. Rev.* **D92** (2015), no. 12 123516, [arXiv:1411.1074].

[2] R. D. Sorkin, *The Statistical Mechanics of Black Hole Thermodynamics*, in *Black Holes and Relativistic Stars* (R. M. Wald, ed.), p. 177, 1998. gr-qc/9705006.

[3] V. Vasileiou, J. Granot, T. Piran, and G. Amelino-Camelia, *A Planck-scale limit on spacetime fuzziness and stochastic Lorentz invariance violation*, *Nature Phys.* **11** (2015), no. 4 344–346.

[4] A. A. Robb, *Geometry of Time and Space*, .

[5] E. C. Zeeman, *Causality implies the lorentz group*, *Journal of Mathematical Physics* **5** (1963), no. 4 490–493.

[6] S. W. Hawking, A. R. King, and P. J. McCarthy, *A new topology for curved spacetime which incorporates the causal, differential, and conformal structures*, *Journal of Mathematical Physics* **17** (1976), no. 2 174.

[7] D. B. Malament, *The class of continuous timelike curves determines the topology of spacetime*, *Journal of Mathematical Physics* **18** (1977), no. 7 1399.

[8] A. Levichev, *On causal structure of homogeneous lorentzian manifolds*, *General Relativity and Gravitation* **21** (1989), no. 10 1027–1045.

[9] J. Myrheim, *STATISTICAL GEOMETRY*, . CERN-TH-2538.

[10] G. ′t Hooft, *Talk given at 8th Conf. on General Relativity and Gravitation, Waterloo, Canada, Aug 7-12, 1977.*, .

[11] L. Bombelli, J. Lee, D. Meyer, and R. D. Sorkin, *Space-time as a causal set*, *Phys. Rev. Lett.* **59** (Aug, 1987) 521–524.

[12] M. Ahmed, S. Dodelson, P. B. Greene, and R. Sorkin, *Everpresent λ*, *Phys. Rev. D* **69** (May, 2004) 103523.

[13] R. D. Sorkin, *Is the cosmological 'constant' a nonlocal quantum residue of discreteness of the causal set type?*, *AIP Conf. Proc.* **957** (2007) 142–153, [arXiv:0710.1675].

[14] F. Dowker, J. Henson, and R. D. Sorkin, *Quantum Gravity Phenomenology, Lorentz Invariance and Discreteness*, *Modern Physics Letters A* **19** (2004) 1829–1840, [gr-qc/0311055].

[15] N. Kaloper and D. Mattingly, *Low energy bounds on Poincaré violation in causal set theory*, *Physical Review D.* **74** (Nov., 2006) 106001, [astro-ph/0607485].

[16] L. Philpott, *FAST TRACK COMMUNICATION: Particle simulations in causal set theory*, *Classical and Quantum Gravity* **27** (Feb., 2010) 042001, [arXiv:0911.5595].

[17] D. P. Rideout and R. D. Sorkin, *Classical sequential growth dynamics for causal sets*, *Physical Review D* **61** (Jan., 2000) 024002, [gr-qc/9904062].

[18] R. D. Sorkin, *On the Role of Time in the Sum-over-histories Framework for Gravity, paper presented to the conference on The History of Modern Gauge Theories, held Logan, Utah, July 1987*, *Int. J. Theor. Phys.* **33** (1994) 523–534.

[19] R. D. Sorkin, *"a modified sum-over-histories for gravity", reported in highlights in gravitation and cosmology: proceedings of the international conference on gravitation and cosmology, goa, india, 14-19 december, 1987, edited by b. r. iyer, ajit kembhavi, jayant v. narlikar, and c. v. vishveshwara, see pages 184-186 in the article by d. brill and l. smolin:, "Workshop on quantum gravity and new directions"* (1988) 183–191.

[20] R. D. Sorkin, *"first steps with causal sets", in r. cianci, r. de ritis, m. francaviglia, g. marmo, c. rubano, p. scudellaro (eds.), general relativity and gravitational physics, Proceedings of the Ninth Italian Conference of the same name, held Capri, Italy,September, 1990* (1991) 68–90.

[21] R. D. Sorkin, *"spacetime and causal sets", in j.c. d'olivo, e. nahmad-achar, m. rosenbaum, m.p. ryan, l.f. urrutia and f. zertuche (eds.), relativity and gravitation: classical and quantum, Proceedings of the SILARG VII Conference, held Cocoyoc, Mexico, December, 1990* (1991) 150–173.

[22] R. D. Sorkin, *"forks in the road, on the way to quantum gravity", talk given at the conference entitled "directions in general relativity", held at college park, maryland, may, 1993*, *Int. J. Th. Phys.* **36** (1997) 2759–2781, [gr-qc/9706002].

[23] M. Ahmed and R. Sorkin, *Everpresent ?. II. Structural stability*, *Phys. Rev.* **D87** (2013), no. 6 063515, [arXiv:1210.2589].

[24] Y. J. Ng and H. van Dam, *A small but nonzero cosmological constant*, *Int. J. Mod. Phys D.* **49** (2001) 2759–2781, [hep-th/9911102].

[25] N. Suzuki, D. Rubin, C. Lidman, G. Aldering, R. Amanullah, K. Barbary, L. F. Barrientos, J. Botyanszki, M. Brodwin, N. Connolly, K. S. Dawson, A. Dey, M. Doi, M. Donahue, S. Deustua, P. Eisenhardt, E. Ellingson, L. Faccioli, V. Fadeyev, H. K. Fakhouri, A. S. Fruchter, D. G. Gilbank, M. D. Gladders, G. Goldhaber, A. H. Gonzalez, A. Goobar, A. Gude, T. Hattori, H. Hoekstra, E. Hsiao, X. Huang, Y. Ihara, M. J. Jee, D. Johnston, N. Kashikawa, B. Koester, K. Konishi, M. Kowalski, E. V. Linder, L. Lubin, J. Melbourne, J. Meyers, T. Morokuma, F. Munshi, C. Mullis, T. Oda, N. Panagia, S. Perlmutter, M. Postman, T. Pritchard, J. Rhodes, P. Ripoche, P. Rosati, D. J. Schlegel, A. Spadafora, S. A. Stanford, V. Stanishev, D. Stern, M. Strovink, N. Takanashi, K. Tokita, M. Wagner, L. Wang, N. Yasuda, H. K. C. Yee, and T. Supernova Cosmology Project, *The Hubble Space Telescope Cluster Supernova Survey. V. Improving the Dark-energy Constraints above $z > 1$ and Building an Early-type-hosted Supernova Sample*, *Astrophys. J* **746** (Feb., 2012) 85, [arXiv:1105.3470].

[26] **BOSS** Collaboration, T. Delubac et al., *Baryon acoustic oscillations in the Ly forest of BOSS DR11 quasars*, *Astron. Astrophys.* **574** (2015) A59, [arXiv:1404.1801].

[27] **BOSS** Collaboration, A. Font-Ribera et al., *Quasar-Lyman α Forest Cross-Correlation from BOSS DR11 : Baryon Acoustic Oscillations*, *JCAP* **1405** (2014) 027, [arXiv:1311.1767].

[28] F. Melia and T. M. McClintock, *Supermassive Black Holes in the Early Universe*, *Proc. Roy. Soc. Lond.* **A471** (2015) 0449, [arXiv:1511.0549].

[29] J. D. Barrow, *A Strong Constraint on Ever-Present Lambda*, *Phys. Rev.* **D75** (2007) 067301, [gr-qc/0612128].

[30] J. A. Zuntz, *The cosmic microwave background in a causal set universe*, *Phys. Rev.* **D77** (2008) 043002, [arXiv:0711.2904].

[31] J. Bell, *On the Einstein-Podolsky-Rosen paradox*, *Physics* **1** (1964) 195.

[32] I. Zlatev, L. Wang, and P. J. Steinhardt, *Quintessence, Cosmic Coincidence, and the Cosmological Constant*, *Physical Review Letters* **82** (Feb., 1999) 896–899, [astro-ph/9807002].

[33] A. Lewis and S. Bridle, *Cosmological parameters from CMB and other data: a Monte- Carlo approach*, *Phys. Rev.* **D66** (2002) 103511, [astro-ph/0205436].

[34] A. Lewis, A. Challinor, and A. Lasenby, *Efficient computation of CMB anisotropies in closed FRW models*, *Astrophys. J.* **538** (2000) 473–476, [astro-ph/9911177].

[35] F. Beutler, C. Blake, M. Colless, D. Jones, L. Staveley-Smith, L. Campbell, Q. Parker, W. Saunders, and F. Watson, *The 6dF Galaxy Survey: baryon acoustic oscillations and the local Hubble constant*, *Mon. Not. R. Astron. Soc* **416** (Oct., 2011) 3017–3032, [arXiv:1106.3366].

[36] L. Anderson, É. Aubourg, S. Bailey, F. Beutler, V. Bhardwaj, M. Blanton, A. S. Bolton, J. Brinkmann, J. R. Brownstein, A. Burden, C.-H. Chuang, A. J. Cuesta, K. S. Dawson, D. J. Eisenstein, S. Escoffier, J. E. Gunn, H. Guo, S. Ho, K. Honscheid, C. Howlett, D. Kirkby, R. H. Lupton, M. Manera, C. Maraston, C. K. McBride, O. Mena, F. Montesano, R. C. Nichol, S. E. Nuza, M. D. Olmstead, N. Padmanabhan, N. Palanque-Delabrouille, J. Parejko, W. J. Percival, P. Petitjean, F. Prada, A. M. Price-Whelan, B. Reid, N. A. Roe, A. J. Ross, N. P. Ross, C. G. Sabiu, S. Saito, L. Samushia, A. G. Sánchez, D. J. Schlegel, D. P. Schneider, C. G. Scoccola, H.-J. Seo, R. A. Skibba, M. A. Strauss, M. E. C. Swanson, D. Thomas, J. L. Tinker, R. Tojeiro, M. V. Magaña, L. Verde, D. A. Wake, B. A. Weaver, D. H. Weinberg, M. White, X. Xu, C. Yèche, I. Zehavi, and G.-B. Zhao, *The clustering of galaxies in the SDSS-III Baryon Oscillation Spectroscopic Survey: baryon acoustic oscillations in the Data Releases 10 and 11 Galaxy samples*, *Mon. Not. R. Astron. Soc* **441** (June, 2014) 24–62, [arXiv:1312.4877].

[37] A. J. Ross, L. Samushia, C. Howlett, W. J. Percival, A. Burden, and M. Manera, *The clustering of the SDSS DR7 main Galaxy sample I. A 4 per cent distance measure at* $z = 0.15$, *Mon. Not. Roy. Astron. Soc.* **449** (2015), no. 1 835–847, [arXiv:1409.3242].

[38] E. A. Kazin et al., *The WiggleZ Dark Energy Survey: improved distance measurements to* $z = 1$ *with reconstruction of the baryonic acoustic feature*, *Mon. Not. Roy. Astron. Soc.* **441** (2014), no. 4 3524–3542, [arXiv:1401.0358].

[39] W. Percival, B. Reid, D. Eisenstein, N. Bahcall, T. Budavari, J. Frieman, M. Fukugita, J. Gunn, Ž. Ivezić, G. Knapp, R. Kron, J. Loveday, R. Lupton, T. McKay, A. Meiksin, R. Nichol, A. Pope, D. Schlegel, D. Schneider, D. Spergel, C. Stoughton, M. Strauss, A. Szalay, M. Tegmark, M. Vogeley, D. Weinberg, D. York, and I. Zehavi, *Baryon acoustic oscillations in the Sloan Digital Sky Survey Data Release 7 galaxy sample*, *Mon. Not. R. Astron. Soc* **401** (Feb., 2010) 2148–2168, [arXiv:0907.1660].

[40] **BOSS** Collaboration, L. Anderson et al., *The clustering of galaxies in the SDSS-III Baryon Oscillation Spectroscopic Survey: baryon acoustic oscillations in the Data Releases 10 and 11 Galaxy samples*, *Mon. Not. Roy. Astron. Soc.* **441** (2014), no. 1 24–62, [arXiv:1312.4877].

[41] N. Padmanabhan, X. Xu, D. Eisenstein, R. Scalzo, A. Cuesta, K. Mehta, and E. Kazin, *A 2 per cent distance to $z = 0.35$ by reconstructing baryon acoustic oscillations - I. Methods and application to the Sloan Digital Sky Survey*, *Mon. Not. R. Astron. Soc* **427** (Dec., 2012) 2132–2145, [arXiv:1202.0090].

[42] I. D. Novikov and K. S. Thorne, *Astrophysics of black holes.*, in *Black Holes (Les Astres Occlus)* (C. Dewitt and B. S. Dewitt, eds.), pp. 343–450, 1973.

[43] X.-B. Wu, F. Wang, X. Fan, W. Yi, W. Zuo, F. Bian, L. Jiang, I. D. McGreer, R. Wang, J. Yang, Q. Yang, D. Thompson, and Y. Beletsky, *An ultraluminous quasar with a twelve-billion-solar-mass black hole at redshift 6.30*, *Nature* **518** (Feb., 2015) 512–515, [arXiv:1502.0741].

[44] B. P. Venemans et al., *The identification of z-dropouts in Pan-STARRS1: three quasars at $6.5 < z < 6.7$*, *Astrophys. J.* **801** (2015), no. 1 L11, [arXiv:1502.0192].

[45] B. D. Fields, *The primordial lithium problem*, *Ann. Rev. Nucl. Part. Sci.* **61** (2011) 47–68, [arXiv:1203.3551].

[46] A. J. Korn, F. Grundahl, O. Richard, P. S. Barklem, L. Mashonkina, R. Collet, N. Piskunov, and B. Gustafsson, *A probable stellar solution to the cosmological lithium discrepancy*, *Nature* **442** (2006) 657–659, [astro-ph/0608201].

[47] M. Pospelov and J. Pradler, *Big Bang Nucleosynthesis as a Probe of New Physics*, *Ann. Rev. Nucl. Part. Sci.* **60** (2010) 539–568, [arXiv:1011.1054].

[48] F.X.Timmes, *BBN code http : //cococubed.asu.edu/code$_p$ages/net$_b$igbang.shtml*, *BBN code http : //cococubed.asu.edu/code$_p$ages/net$_b$igbang.shtml Cococubed.com* (-).

[49] S. Burles and D. Tytler, *The Deuterium abundance toward QSO 1009+2956*, *Astrophys. J.* **507** (1998) 732–744, [astro-ph/9712109].

[50] D. Kirkman, D. Tytler, N. Suzuki, J. M. O'Meara, and D. Lubin, *The Cosmological baryon density from the deuterium to hydrogen ratio towards QSO absorption systems: D/H towards Q1243+3047*, *Astrophys. J. Suppl.* **149** (2003) 1, [astro-ph/0302006].

[51] R. J. Cooke, M. Pettini, K. M. Nollett, and R. Jorgenson, *The Primordial Deuterium Abundance of the Most Metal-poor Damped Lyman-α System*, *Astrophys. J.* **830** (Oct., 2016) 148, [arXiv:1607.0390].

[52] T. M. Bania, R. T. Rood, and D. S. Balser, *The cosmological density of baryons from observations of $^3He^+$ in the Milky Way*, *Nature* **415** (Jan., 2002) 54–57.

[53] L. Sbordone, P. Bonifacio, E. Caffau, H.-G. Ludwig, N. T. Behara, J. I. González Hernández, M. Steffen, R. Cayrel, B. Freytag, C. van't Veer, P. Molaro, B. Plez, T. Sivarani, M. Spite, F. Spite, T. C. Beers, N. Christlieb, P. François, and V. Hill, *The metal-poor end of the Spite plateau. I. Stellar parameters, metallicities, and lithium abundances*, *Astron. Astrophys.* **522** (Nov., 2010) A26, [arXiv:1003.4510].

[54] P. Bonifacio et al., *The lithium content of the globular cluster ngc 6397*, *Astron. Astrophys.* **390** (2002) 91, [astro-ph/0204332].

[55] S. G. Ryan, J. E. Norris, and T. C. Beers, *The spite lithium plateau: ultrathin but post primordial*, *Astrophys. J.* **523** (1999) 654–677, [astro-ph/9903059].

[56] K. A. Olive and E. D. Skillman, *A Realistic determination of the error on the primordial helium abundance: Steps toward non-parametric nebular helium abundances*, *Astrophys. J.* **617** (2004) 29, [astro-ph/0405588].

[57] C. R. Contaldi, F. Dowker, and L. Philpott, *Polarization diffusion from spacetime uncertainty*, *Classical and Quantum Gravity* **27** (2010), no. 17 172001.

[58] L. Philpott, F. Dowker, and R. D. Sorkin, *Energy-momentum diffusion from spacetime discreteness*, *Phys.Rev.D* **79** (June, 2009) 124047, [arXiv:0810.5591].

[59] L. Philpott, F. Dowker, and R. Sorkin, *Massless particle diffusion in causal set theory*, *Journal of Physics: Conference Series* **174** (2009), no. 1 012048.

[60] R. D. Sorkin, *Does Locality Fail at Intermediate Length-Scales*, *ArXiv General Relativity and Quantum Cosmology e-prints* (Mar., 2007) [gr-qc/0703099].

[61] L. Bombelli, J. Noldus, and J. Tafoya, *Lorentzian Manifolds and Causal Sets as Partially Ordered Measure Spaces*, *ArXiv e-prints* (Dec., 2012) [arXiv:1212.0601].

[62] S. Surya, *Directions in Causal Set Quantum Gravity*, *ArXiv e-prints* (Mar., 2011) [arXiv:1103.6272].

[63] L. Bombelli and D. A. Meyer, *The origin of Lorentzian geometry*, *Physics Letters A* **141** (Nov., 1989) 226–228.

[64] R. D. Sorkin, *Causal Sets: Discrete Gravity (Notes for the Valdivia Summer School)*, *ArXiv General Relativity and Quantum Cosmology e-prints* (Sept., 2003) [gr-qc/0309009].

[65] L. Bombelli, *Statistical Lorentzian geometry and the closeness of Lorentzian manifolds*, *Journal of Mathematical Physics* **41** (Oct., 2000) 6944–6958, [gr-qc/0002053].

[66] L. Bombelli and J. Noldus, *The moduli space of isometry classes of globally hyperbolic spacetimes*, *Classical and Quantum Gravity* **21** (Sept., 2004) 4429–4453, [gr-qc/0402049].

[67] G. Brightwell, J. Henson, and S. Surya, *A 2D model of causal set quantum gravity: the emergence of the continuum*, *Classical and Quantum Gravity* **25** (May, 2008) 105025, [arXiv:0706.0375].

[68] O. Aharony, O. Bergman, D. L. Jafferis, and J. Maldacena, *Script $N = 6$ superconformal Chern-Simons-matter theories, M2-branes and their gravity duals*, *Journal of High Energy Physics* **10** (Oct., 2008) 091, [arXiv:0806.1218].

[69] S. Surya, *Causal Set Topology*, *ArXiv e-prints* (Dec., 2007) [arXiv:0712.1648].

[70] R. D. Sorkin, *Finitary substitute for continuous topology*, *International Journal of Theoretical Physics* **30** (1991), no. 7 923–947.

[71] L. Bombelli, J. Lee, D. Meyer, and R. D. Sorkin, *Space-time as a causal set*, *Phys. Rev. Lett.* **59** (Aug, 1987) 521–524.

[72] M. Ahmed, S. Dodelson, P. B. Greene, and R. Sorkin, *Everpresent λ*, *Phys. Rev. D* **69** (May, 2004) 103523.

[73] G. Aad, T. Abajyan, B. Abbott, J. Abdallah, S. Abdel Khalek, A. A. Abdelalim, O. Abdinov, R. Aben, B. Abi, M. Abolins, and et al., *Observation of a new particle in the search for the Standard Model Higgs boson with the ATLAS detector at the LHC*, *Physics Letters B* **716** (Sept., 2012) 1–29, [arXiv:1207.7214].

[74] S. Chatrchyan, V. Khachatryan, A. M. Sirunyan, A. Tumasyan, W. Adam, E. Aguilo, T. Bergauer, M. Dragicevic, J. Erö, C. Fabjan, and et al., *Observation of a new boson at a mass of 125 GeV with the CMS experiment at the LHC*, *Physics Letters B* **716** (Sept., 2012) 30–61, [arXiv:1207.7235].

[75] N. Zwane, *Long-Lived Particle Searches in R-Parity Violating MSSM*, *arXiv:1505.03479* (May, 2015) [arXiv:1505.0347].

[76] R. M. Dudley, *Lorentz-invariant Markov processes in relativistic phase space*, *Arkiv for Matematik* **6** (Jan., 1966) 241–268.

[77] R. D. Sorkin, *Stochastic evolution on a manifold of states*, *Annals of Physics* **168** (Apr., 1986) 119–147.

[78] F. Dowker, *Causal set phenomenology*, .

[79] J. Stricker, *Using the sachs-wolfe effect to limit dark energy*, *Physics 317 Cosmology notes* (2006).

[80] M. LoVerde and N. Afshordi, *Extended Limber Approximation*, *Phys. Rev.* **D78** (2008) 123506, [arXiv:0809.5112].

[81] K. Mehta, A. Cuesta, X. Xu, D. Eisenstein, and N. Padmanabhan, *A 2 per cent distance to $z = 0.35$ by reconstructing baryon acoustic oscillations - III. Cosmological measurements and interpretation*, *Mon. Not. R. Astron. Soc* **427** (Dec., 2012) 2168–2179, [arXiv:1202.0092].

[82] J.-X. Li, F.-Q. Wu, Y.-C. Li, Y. Gong, and X.-L. Chen, *Cosmological constraint on Brans-Dicke Model*, *Res. Astron. Astrophys.* **15** (2015), no. 12 2151–2163, [arXiv:1511.0528].

[83] A. Coc, J.-P. Uzan, and E. Vangioni, *Standard Big-Bang Nucleosynthesis after Planck*, arXiv:1307.6955.

[84] S. G. Ryan, T. C. Beers, K. A. Olive, B. D. Fields, and J. E. Norris, *Primordial lithium and big bang nucleosynthesis*, astro-ph/9905211.

[85] J. M. O'Meara, S. Burles, J. X. Prochaska, G. E. Prochter, R. A. Bernstein, and K. M. Burgess, *The Deuterium to Hydrogen Abundance Ratio Towards the QSO SDSS1558-0031*, *Astrophys. J.* **649** (2006) L61–L66, [astro-ph/0608302].

[86] M. Pettini and R. Cooke, *A new, precise measurement of the primordial abundance of deuterium*, *Mon. Not. R. Astron. Soc* **425** (Oct., 2012) 2477–2486, [arXiv:1205.3785].

[87] Y. I. Izotov and T. X. Thuan, *The Primordial Abundance of ^{4}He Revisited*, *Astrophys. J.* **500** (June, 1998) 188–216.

[88] A. Peimbert, M. Peimbert, and V. Luridiana, *Temperature bias and the primordial helium abundance determination*, *Astrophys. J.* **565** (2002) 668, [astro-ph/0107189].

[89] Y. I. Izotov and T. X. Thuan, *Systematic effects and a new determination of the primordial abundance of He-4 and dY/dZ from observations of blue compact galaxies*, *Astrophys. J.* **602** (2004) 200–230, [astro-ph/0310421].

[90] M. Fukugita and M. Kawasaki, *Primordial helium abundance: a reanalysis of the izotov-thuan spectroscopic sample*, *Astrophys. J.* **646** (2006) 691–695, [astro-ph/0603334].

[91] R. K. Sachs and A. M. Wolfe, *Perturbations of a cosmological model and angular variations of the microwave background*, *Astrophys. J.* **147** (1967) 73–90. [Gen. Rel. Grav.39,1929(2007)].

[92] M. LoVerde and N. Afshordi, *Extended Limber Approximation*, *Phys. Rev.* **D78** (2008) 123506, [arXiv:0809.5112].

[93] V. Mukhanov, *Physical Foundations of Cosmology*. Cambridge University Press, Oxford, 2005.

[94] Y. K. Yazdi and A. Kempf, *Towards spectral geometry for causal sets*, *Classical and Quantum Gravity* **34** (May, 2017) 094001, [arXiv:1611.0994].

[95] N. Zwane, N. Afshordi, and R. D. Sorkin, *Cosmological Tests of Everpresent* Λ, arXiv:1703.0626.

Appendix A

Box Operator

The causal set D'Alembert operator first introduced by Sorkin[60] is non-local. $B_\epsilon\phi(x)$ is a sum of $\phi(y)$, for all y's in the past of the point x, each term weighted differently in the sum. The weight depends on the spacetime interval volume between x and y, $I(x,y)$. The interval volume is the number of causal elements between x and y. We denote N_n to be intervals with n elements. In full Minkowski spacetime N_n is infinite.

$$N_n = \int_{y\prec x} \sqrt{-g}\rho \frac{(\rho V(x,y))^n}{n!} e^{-\rho V(x,y)} d^D y \tag{A.1}$$

For a diamond in Minkowsk with volume $V_M = 1$, when x, is the upper-corner of the diamond

$$N_n = \int_0^1 du \int_0^1 dv \rho \frac{(\rho(1-v)(1-u))^n}{n!} e^{-\rho(1-v)(1-u)} \tag{A.2}$$

In the causal sets box, the zeroth neighbors have different contribution from the 1st neighbors, which also differ from the 2nd neighbor and so. The box is defined as

$$\begin{aligned} B\phi(x) &= \alpha_2 \ell^{-2}\phi(x) + \beta_2 \ell^{-4} \int dy^2\, \phi(y) \sum_{i=1}^{n_d} C_i^{(d)} \frac{(V_d(y)\ell^{-2})^{i-1}}{(i-1)!} e^{-uv\ell^{-2}} \\ &= \alpha_2 \ell^{-2}\phi(x) + \beta_2 \ell^{-2} \int dy^2\, \phi(y) \sum_{i=1}^{n_d} C_i^{(d)} N_n(x,n) \\ &= \alpha_2 \ell^{-2}\phi(x) + \beta_2 \ell^{-4} \int du \int dv\, \phi(y) \left(1 - 2\ell^{-2}uv + \frac{\ell^{-2}}{2}(uv)^2\right) e^{-uv\ell^{-2}} \end{aligned}$$

Taylor expand $\phi(y)$

$$
\begin{aligned}
B\phi(x) &= \alpha_2\ell^{-2}\phi(x) + \beta_2\ell^{-4}\int_a^0 du\int_b^0 dv\, e^{-uv\ell^{-2}}\left(1-2\ell^{-2}uv+\frac{\ell^{-2}}{2}(uv)^2\right)\\
&\quad\times\left(1+u\partial_u+v\partial_v+\frac{u^2+v^2}{4}(\partial_u^2+\partial_v^2)+uv\partial_u\partial_v\right)\phi(0)\\
&= \alpha_2\ell^{-2}\phi(x)+\beta_2\ell^{-4}\left(\frac{1}{2}\left(\ell^2+e^{-ab/\ell^2}(ab-\ell^2)\right)\phi(0)+\frac{1}{2}ab^2e^{-ab/\ell^2}\partial_v\phi(0)\right.\\
&\quad+\frac{1}{2}a^2be^{-ab/\ell^2}\partial_u\phi(0)+\frac{1}{2}\left(-\ell^4+e^{-ab/\ell^2}(a^2b^2+ab\ell^2+\ell^4)\partial_v\partial_u\phi(0)\right)\\
&\quad\left.+\frac{1}{4}\left(\frac{\partial_u^2}{b^2}+\frac{\partial_v^2}{a^2}\right)\phi(0)e^{-ab/\ell^2}\left(a^3b^3+a^2b^2\ell^2+2ab\ell^4-2\left(-1+e^{ab/\ell^2}\right)\ell^6\right)\right)\\
&\xrightarrow[a\to\infty]{b\to\infty}\alpha_2\ell^{-2}\phi(0)+\beta_2\left(\frac{\ell^{-2}}{2}\phi(0)-\frac{1}{2}\partial_v\partial_u\phi(0)\right)\\
&= \alpha_2\ell^{-2}\phi(0)+\beta_2\frac{\ell^{-2}}{2}\phi(0)-\frac{\beta_2}{4}\left(-\partial_t^2+\partial_x^2\right)\phi(0) \qquad \text{(A.3)}
\end{aligned}
$$

For $B\phi(x)\approx\Box\phi(x)=-\frac{\partial^2}{\partial t^2}+\frac{\partial^2}{\partial x^2}$, $\beta_2=4$ and $\alpha_2=-2$.

In simulation we have a cut-off in u and v so that the known B_k has cut-off corrections, For a 2D Minkowski spacetime $V_d=uv$,

$$
\begin{aligned}
B\phi(x) &= -2\epsilon\ell^{-2}\phi(x)+4\epsilon^2\ell^{-4}\int du\int dv\,\phi(y)\left(\sum_{n=1}^{\infty}f_\epsilon(n)\frac{(V_d(y)\ell^{-2})^{n-1}}{(n-1)!}\right)e^{-uv\ell^{-2}} \qquad \text{(A.4)}\\
&= -2\epsilon\ell^{-2}\phi(x)+4\epsilon^2\ell^{-4}\int du\int dv\,\phi(y)e^{-uv\epsilon\ell^{-2}}\left(1-2\ell^{-2}uv\epsilon+\frac{\ell^{-4}}{2}(uv\epsilon)^2\right) \qquad \text{(A.5)}\\
&= -2\ell^{-2}\phi(x)+4\ell^{-4}\int du\int dv\,\phi(y)e^{-uv\ell^{-2}}\left(1-2\ell^{-2}uv+\frac{\ell^{-4}}{2}(uv)^2\right) \qquad \epsilon\to 1 \qquad \text{(A.6)}
\end{aligned}
$$

Assume $\phi(u,v)$ is a solution of the box operator then $B\phi(x)=0$

$$
\begin{aligned}
B\phi(x) &= -2\ell^{-2}\phi(x)+4\ell^{-4}\int du\int dv\,\phi(y)e^{-uv\ell^{-2}}\left(1-2\ell^{-2}uv+\frac{\ell^{-4}}{2}(uv)^2\right)=0 \qquad \text{(A.7)}\\
\phi(x) &= 2\ell^{-2}\int du\int dv\,\theta(u)\theta(v)\phi(y)e^{-uv\ell^{-2}}\left(1-2\ell^{-2}uv+\frac{\ell^{-4}}{2}(uv)^2\right) \qquad \text{(A.8)}
\end{aligned}
$$

Let $\phi(u,v) = A$,

$$\phi(x) = 2\ell^{-2}\int du \int dv\, \theta(u)\theta(v) A e^{-uv\ell^{-2}} \left(1 - 2\ell^{-2}uv + \frac{\ell^{-4}}{2}(uv)^2\right) \tag{A.9}$$

$$= 2\ell^{-2}A\left(\frac{1}{2}e^{-u_0v_0\ell^{-2}}u_0v_0 + \frac{\ell^2}{2} - \frac{1}{2}e^{-u_0v_0\ell^{-2}}\ell^2\right) \tag{A.10}$$

$$= 2\ell^{-2}A\frac{\ell^2}{2} \qquad \{u_0, v_0\} \to \infty \tag{A.11}$$

$$= A \tag{A.12}$$

Let $\phi(u,v) = e^{-v^2}$,

$$\phi(x) = 2\ell^{-2}\int du \int dv\, \theta(u)\theta(v))e^{-v^2}e^{-uv\ell^{-2}} \left(1 - 2\ell^{-2}uv + \frac{\ell^{-4}}{2}(uv)^2\right) \tag{A.13}$$

$$\begin{aligned} = 2\ell^{-2}\Bigg(&\frac{1}{2}u_0\Bigg[\frac{u_0}{\ell^2}\Bigg(\left(\frac{1}{2} - \frac{1}{4\ell^2}e^{u_0^2/4\ell^4}\sqrt{u_0}\mathrm{Erfc}\left[u_0/2\ell^2\right]\right)(1-\theta(v_0)) \\ &+\frac{1}{4\ell^2}e^{u_0^2/4\ell^4}\left(2\ell^2 e^{-\frac{(u_0+2v_0\ell^2)^2}{4\ell^4}} - \sqrt{\pi}u_0\mathrm{Erfc}\left[v_0 + \frac{u_0}{2\ell^2}\right]\right)\theta(v_0)\Bigg) \\ &+\ e^{\frac{u_0}{4\ell^4}}\sqrt{\pi}\left(-\mathrm{Erfc}\left[\frac{u_0}{2\ell^2}\right] + \left(-\mathrm{Erfc}\left[v_0 + \frac{u_0}{2\ell^2}\right] + \mathrm{Erfc}\left[\frac{u_0}{2\ell^2}\right]\right)\theta(v_0)\right)\Bigg]\Bigg) \end{aligned} \tag{A.14}$$